



Contents lists available at ScienceDirect

## Tectonophysics

journal homepage: [www.elsevier.com/locate/tecto](http://www.elsevier.com/locate/tecto)

## African stress pattern from formal inversion of focal mechanism data

Damien Delvaux <sup>a,\*</sup>, Andreas Barth <sup>b</sup><sup>a</sup> Royal Museum for Central Africa, Tervuren, Belgium<sup>b</sup> Heidelberg Academy of Sciences and Humanities; Geophysical Institute, University of Karlsruhe, Germany

## ARTICLE INFO

## Article history:

Received 23 January 2009

Received in revised form 7 May 2009

Accepted 15 May 2009

Available online 20 May 2009

## Keywords:

Africa

Tectonic stress

Focal mechanisms

East African Rift System

Intraplate forces

## ABSTRACT

The kinematic models and the associated orientation of extensional stress of the East African Rift System have been subjected to much debate since a long time. In the past decades, the proposed models relied on the interpretation of the overall rift geometry, geological fault-slip data and the few focal mechanisms available. These models generally suffer of a poor time control and an underestimation of the possible changes in the stress field and geodynamic regime with time and space. In the recent years, there has been a significant increase in the number of focal mechanisms available for the entire rift system, and it is now possible to estimate the present-day stress field in relative detail based on seismotectonic data alone.

We compile 347 focal mechanism data from the Global/Harvard CMT catalogue and various other sources and grouped 332 of them in 24 distinct regions (boxes) on the basis of their geographical proximity, kinematic homogeneity and tectonic setting. For each box and for the same data set, reduced stress tensors have been obtained by formal stress inversion using both the TENSOR program (Delvaux & Sperner, 2003) and the SLICK method (Michael, 1984/1987). Both inversion methods show in comparable results in terms of horizontal stress axes orientations and tectonic stress regimes, which stem for the robustness of the approach. The obtained stress pattern reflects a complex interaction between 1st order effects as different driving forces, including plate boundary forces, and 2nd and 3rd order effects as gravitational potential of topography, intra-lithospheric processes, and the influence of structural heterogeneities of the rift structures.

The evidence present in the stress orientations of the 2nd and 3rd order stress pattern as the variations in the horizontal stress axes along the axis of the rift are of particular interest as they were not yet captured or shown in earlier numerical models of the stress field. Additional sources of tectonic forces in supplement to the gravitational potential energy forces as considered in the earlier models are necessary to explain the observed patterns.

© 2009 Elsevier B.V. All rights reserved.

## 1. Introduction

The 2nd and 3rd order patterns of intraplate stress field are becoming recognized in the continental plates with improved data interpretation and spatial coverage. The lack of data has always been a problem in East Africa and impeded adequate tectonic interpretation. The new focal mechanism data and their analysis presented here allow and facilitate a revisiting of the tectonic interpretations of the stress field patterns. The 2nd and 3rd order stress patterns obtained as the result of formal stress inversion of illustrated focal mechanism solutions reveal many interesting “complications” in the stress field that were not captured by large-scale numerical models of previous studies. The results presented here intend to lay the foundation for constraints on higher detailed, local, high-resolution numerical models that will help to differentiate between the various sources of the 2nd and 3rd order stress field.

In the absence of continental gravitational potential energy (PE) forces, the entire African plate would be expected to be in compression, due to the surrounding ridge push forces (Fig. 1). Within most of the African plate (except for the Mediterranean region and Western Africa), those PE forces are dominated by the effect of the East African Rift System (EARS).

The East African Rift System is an example of the relatively rare instance of active continental rifting. Passing for nearly 3000 km through the continent, the EARS separates the Nubian subplate to the west from the Somali subplate to the east (Fig. 1). Beginning in the Afar triple junction, it crosses the Ethiopian highland, forms the Gregory Rift in Kenya and disperses in northern Tanzania after Lake Natron, forming the Eastern Rift Branch. Grimison and Chen (1988) proposed an extended Eastern Branch that connects to the Davie Ridge along the continental margin on the Indian Ocean coast of East-Africa to explain the seismic activity in the northern Mozambique Channel. The Western Rift Branch starts in southern Sudan and runs through the rift valley lakes – including Lakes Tanganyika and Malawi – to Mozambique. The southern end of the EARS is less clear and its connection to the Southwest Indian Ridge is still controversial (Horner-Johnson et al.,

\* Corresponding author.

E-mail addresses: [damiendelvaux@africamuseum.be](mailto:damiendelvaux@africamuseum.be) (D. Delvaux), [Andreas.Barth@gpi.uni-karlsruhe.de](mailto:Andreas.Barth@gpi.uni-karlsruhe.de) (A. Barth).

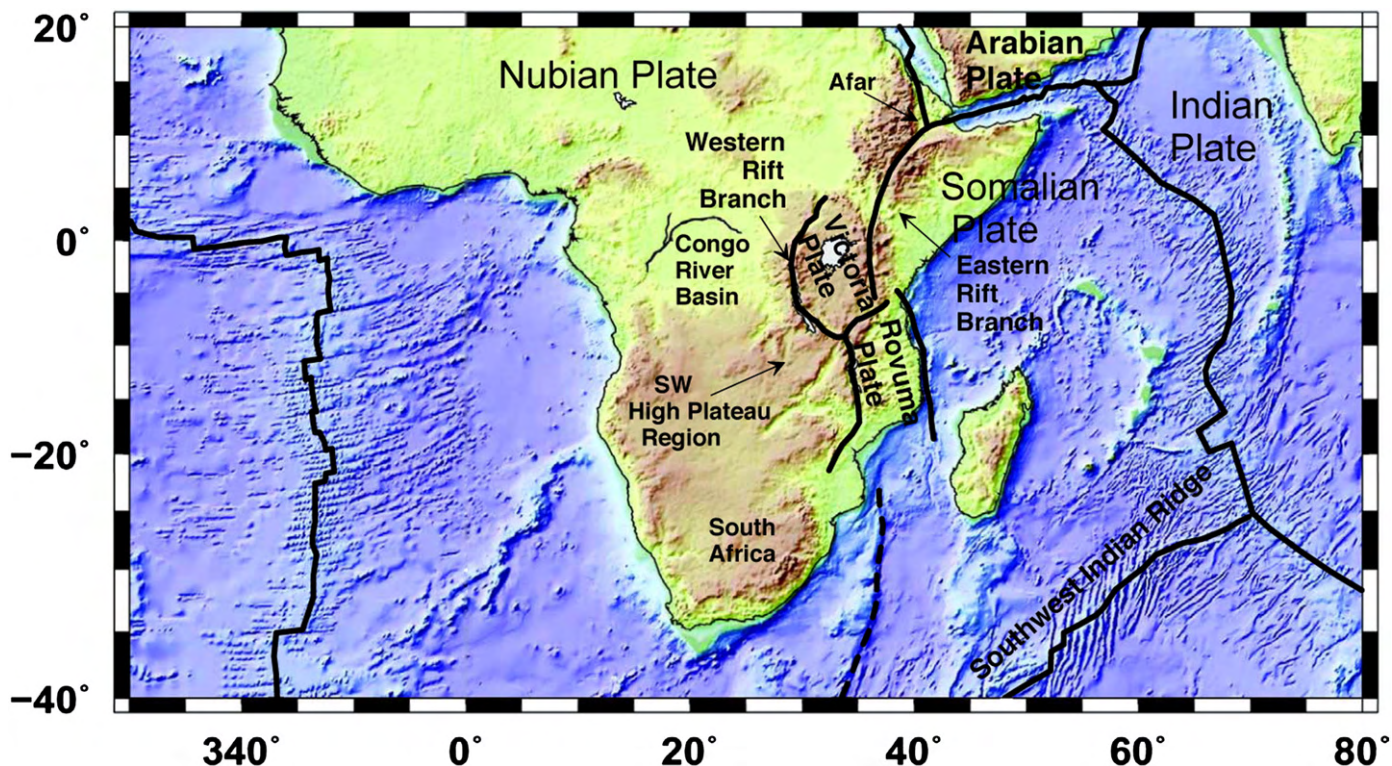


Fig. 1. General setting of the East African Rift System (EARS) with colour-coded topography as background. The two major branches of the EARS – the Eastern Rift Branch and the Western Rift Branch – separate the Nubian plate from the Somalian plate and isolate the two small Victoria and Rovuma plates in between (plate definition as in Calais et al., 2006). Thick lines are plate boundaries.

2005; Lemaux et al., 2002). Chu and Gordon (1999) used seafloor-spreading rates to determine the Euler pole of rotation between the Nubian and the Somalian subplate in the southern Mozambique Channel. Hence, the tectonic regime changes from extension north of the pole to compression south of it.

The opening kinematics of the EARS has been the focus of investigations since decades. In the absence of sufficient earthquake focal mechanism data, the kinematic models were first proposed on the basis of a geometrical interpretation of the large-scale tectonic structures interpreted from remote-sensing imagery (Chorowicz & Mukonki, 1980; Kazmin, 1980). These models were soon supplemented by paleostress inversion of geological fault-slip data collected along the major faults bordering the rift depressions (Tiercelin et al., 1988; Chorowicz, 1989). This approach suffers an insufficient timing control, as the fault-slip data have often been measured in basement rocks along the supposedly active faults. It was later shown that most of the measured data could belong to past tectonic events unrelated to the present rifting dynamics, hence highlighting the importance of stress field fluctuation through geological time (Strecker et al., 1990; Bosworth et al., 1992; Delvaux et al., 1992; Ring et al., 1992; Delvaux, 1993; Bosworth and Strecker, 1997). Such time fluctuation of stress field is also supported by independent observations from seismic profiling in the rift lakes (Morley et al., 1999) and other field-based studies (Le Gall et al., 2005; Nicholas et al., 2007). Recently, kinematic models based on GPS geodesy have been proposed (Fernandez et al., 2004; Calais et al., 2006; Stamps et al., 2008), but due to the small number of permanent GPS stations used, they are not yet able to resolve the plate motions with sufficient details. In the meantime, the knowledge of low magnitude focal mechanisms in regions off-side the main rift zone gives the opportunity to invert for the regional stress field (Barth and Wenzel, 2010). During the last 10 years, the number of available focal mechanisms available for East Africa has increased considerably due to a longer observation time, improvement of the seismic network, installation of local seismic networks and more detailed calculation procedures.

As a result, it is now possible to image the second order – and locally the third order – pattern of tectonic stress for large regions of the EARS and adjacent parts of the African Continent, evidencing the lateral variability of the present-day stress field.

In this paper, first we compile all presently available well constrained single focal mechanism data up to September 2008 (336 single events and 1 composite event). We then group the data into 24 distinct regions (boxes) in function of the geographic proximity and the general tectonic structure and we perform a formal inversion in order to determine the present-day stress field. We compare the results obtained by two different methods (TENSOR program of Delvaux & Sperner, 2003) and SLICK method of Michael, 1984, 1987) for the same boxes and datasets. We also discuss the possible sources for the observed tectonic stress pattern.

## 2. Data compilation

Source mechanisms in East-Africa were examined by several studies using both first motion analysis (e.g. Fairhead and Girdler, 1971) and waveform inversion. The Global CMT Project – formerly Harvard-CMT (Dziewonski et al., 1987) – routinely determines focal mechanisms by moment tensor inversion of both long period body- and surface-waves. The global level of completeness for CMT-solutions is approximately  $M_W \sim 5.5$  (Arvidsson and Ekström, 1998), whereas it is lowered to  $M_W \sim 5.1$  for East-Africa, including events as low as  $M_W = 4.7$ . Thus for strong and most of moderate magnitude events the CMT-solution is given. Foster and Jackson (1998) performed a P- and SH-waveform inversion to calculate source mechanisms from 1966 to 1997 with magnitudes  $M_W \geq 5.1$ . To examine focal mechanisms of three small to minor magnitude events on the Western Branch ( $M_W = 2.0\text{--}3.3$ ), Ferdinand and Arvidsson (2002a) used data of a mobile station network to perform a body waveform inversion. Barth et al. (2007) determined focal mechanisms for events with magnitudes  $4.4 \leq M_W \leq 5.5$  from 1995 to

2002 that were not given by CMT-solutions. Since East-African seismicity is mainly focused on the EARS, especially higher magnitude events seldom occur beside the rift structures. Thus also focal mechanism information concentrates on the rift itself, whereas lower magnitude events with unknown source mechanisms tend to spread on regions neighbouring the rift (Fig. 1). Therefore it is important to use low magnitude focal mechanism solutions in East-Africa for the inversion of the apparent stress field and the understanding of the recent tectonics.

In this study we combine CMT solutions and recent focal mechanism determinations to perform stress inversions for separate regions and discuss the results in terms of East-African tectonics. In total 347 focal mechanisms are chosen for our study (Table 1). The greatest number is taken from the Global CMT catalogue (formerly Harvard CMT) that provides 240 mechanisms from 1977 until September 2008 within the study region. Beside this, additional mechanisms calculated by moment tensor inversion are used to invert for the regional stress field in East-Africa: 38 low magnitude focal mechanisms by Barth et al. (2007), 12 focal mechanisms determined from Tanzanian Broadband Seismic Experiment (Brazier et al., 2005), 23 very-low magnitude mechanisms from the local Mbeya seismic network by Ferdinand and Arvidsson (2002b) and high magnitude focal mechanisms of strong events from 1928 to 1977 (Shudofsky (1985) (12); Foster and Jackson (1998) (10); Kebede and Kulhanek (1991) (5); Grimison and Chen (1988) (1); Doser and Yarwood (1991) (1); Fairhead and Stuart (1982) (1); Nyblade and Langston (1995) (1)). One composite focal mechanism from Ibs-von Seht et al. (2001) has been included for the Lake Magadi region in South Kenya, a region lacking high magnitude seismicity. The two first focal mechanisms that were determined for the East African Rift (graphical construction, De Bremaeker, 1956) were also included. Some of the CMT focal mechanisms have also been studied by others: 2 from the Congo River Basin (Ayele 2002) and 4 from South Sudan (Gaulon et al., 1992); but their CMT solutions were preferred.

In the compiled database (Table 1), the individual focal mechanisms are given with their horizontal stress axes  $S_{Hmax}$  and  $S_{Hmin}$  computed according to Lund and Townend (2007) and stress regime according to the WSM standard (NF: normal faulting, SS: strike-slip faulting, TF: thrust faulting regimen, NS: intermediate between NF and SS, TS: intermediate between SS and TF, U: unknown or oblique).

### 3. Zonation and Box definition

Since the focal mechanism data are not consistent in terms of stress regime and stress orientation over the entire East-Africa and thus cannot be inverted altogether (Barth, 2007), we divide the region into sub-areas (boxes) to study regional changes in stress orientation. For this purpose the zonation of the Global Seismic Hazard Assessment Program (GSHAP) is applied as a starting point. These world-wide zonations take into account the recent and historic seismicity and hence define areas with a common seismic risk (Giardini, 1999; Midzi et al., 1999). This initial zonation was adapted in function of the data set available and the major tectonic structures. From a total of 347 data, we can assemble 332 of them into 24 boxes (Table 1, Fig. 2, 3), on the basis of their geographical proximity and of the tectonic setting from southern Red Sea in the north to southern South Africa, and from the Congo River Basin in the west to the Gulf of Aden and Madagascar in the east.

### 4. Tectonic stress inversion

To study the recent stress field for East Africa we perform formal stress inversions of the given focal mechanisms following two different techniques: the TENSOR program (Delvaux and Sperner, 2003) and the SLICK method (Michael, 1984, 1987). Both attempts rely on two major assumptions for the study region: (a) the stress field is uniform and invariant in space and time, and (b) earthquake slip  $d$  occurs in the direction of maximum shear stress  $\tau$  (Wallace–Bott

hypothesis, Bott, 1959). The angle between the calculated shear stress  $\tau$  and the slip vector  $d$  is the fit angle  $\alpha$ . Thus, the corresponding misfit function to be minimised for each earthquake  $i$  is the misfit angle  $\alpha$ :

$$f(i) = \alpha(i) \quad (1)$$

We use two different inversion techniques to determine the four parameters of the reduced stress tensor that models best the state of stress of a given region: the orientation of the three orthogonal principal stress axes  $\sigma_1$ ,  $\sigma_2$  and  $\sigma_3$  (where  $\sigma_1 \geq \sigma_2 \geq \sigma_3$ ) and the stress ratio  $R$ :

$$R = \sigma_2 - \sigma_3 / \sigma_1 - \sigma_3 \quad (2)$$

which expresses the magnitude of  $\sigma_2$  relative to the magnitudes of  $\sigma_1$  and  $\sigma_3$ .

With Win-Tensor, the new Windows version of the TENSOR program (available online at: <http://users.skynet.be/damien.delvaux/Tensor/tensor-index.html>), we process the data interactively, first using the “Right Dihedron Method”, a graphical method for determination of the range of possible orientations  $\sigma_1$  and  $\sigma_3$ , which is independent from the choice of the nodal planes (Angelier and Mechler, 1984). The initial result is used as a starting point for the iterative grid-search “Rotational Optimisation” procedure using the misfit function F5 in the TENSOR program (described as f3 in Delvaux and Sperner, 2003). It minimises the misfit angle  $\alpha$  (Eq. (1)) using the stress tensor that is being tested, but also favours higher shear stress magnitudes  $|\tau(i)|$  and lower normal stress magnitudes  $|\nu(i)|$  on the plane in order to promote slip. It contains three terms and is implemented in a way that it ranges from 0 (optimal misfit) to 360 and is independent from the ratio  $\sigma_3/\sigma_1$ . The first term that minimises  $\alpha$  is based on the Function S4 of Angelier (1991):

$$f(i) = \sin^2(\alpha(i) / 2) \quad (3)$$

and is dominant over the two others (see Delvaux and Sperner, 2003 for details).

First we invert both nodal planes for each focal mechanism to a stress tensor. Then the plane that is best explained by the stress tensor is selected from the two nodal planes (smaller value of function F5 in Tensor or f3 in Delvaux and Sperner, 2003) and considered as the actual fault (or focal) plane. After this separation, the final inversion then includes only the focal planes that are best fitted by a uniform stress field (Gephart and Forsyth, 1984). The graphical output of the stress tensor in an equal-area projection allows evaluating the overall quality of the result (Fig. 4). The detailed results obtained using TENSOR are provided in Table 2a and b (upper row for each box).

For the formal stress inversion after the SLICK method of Michael (1984) we also take into account the ambiguity between focal and auxiliary plane of the source mechanism by inverting both nodal planes as if they were independent data. Again, in a second step the worse fitted auxiliary planes are removed. The difference between the SLICK inversion routine and other inversion methods is the linearization of the inversion problem that massively reduces the computing time and does not need any starting model that is necessary for non-linear inversions. To linearize the inversion, it is assumed that similar magnitudes of shear stress  $|\tau|$  are present on each inverted fault. If only relative shear stress magnitudes are regarded, the optimum shear stress magnitude can be set a priori to one, so the inversion additionally minimises for:

$$f(i) = (|\tau(i)| - 1)^2. \quad (4)$$

Hence, the inversion after Michael minimises for both, the difference between slip direction  $d$  and direction of maximum shear stress  $\tau$  on one hand (Eq. (1)) and the difference between the shear stress magnitudes  $|\tau|$  on the other hand (Eq. (4), Table 2a). If however,

**Table 1**

Compiled data base of focal mechanisms used in this study, grouped in 24 boxes.

Date–time group Event	Location			Data				SH		Stress Reg.	Source
	Long	Lat	Depth	$M_w$	Strike	Dip	Slip	Max	Min		
<i>Red Sea (box 1)</i>											
EA19670313–19:22:00–Keb	38.80	19.70	2	5.6	309	45	–100	136	046	NF	Kebede & K. 1991
EA19771228–02:45:44–Har	40.32	15.97	10	6.6	106	66	–171	149	059	SS	Harvard CMT
EA19780117–15:00:35–Har	40.49	17.51	15	5.4	282	90	180	147	057	SS	Harvard CMT
EA19800114–04:11:01–Har	40.53	17.12	15	6.0	024	76	–009	161	071	SS	Harvard CMT
EA19800114–12:28:29–Har	40.12	16.99	15	5.7	301	90	180	166	076	SS	Harvard CMT
EA19881210–17:33:25–Har	41.10	16.56	15	5.6	339	74	–017	117	027	SS	Harvard CMT
EA19930312–04:24:21–Har	38.34	19.39	15	5.3	148	31	–083	144	054	NF	Harvard CMT
EA19930312–23:32:52–Har	38.68	19.76	15	5.0	321	45	–090	141	051	NF	Harvard CMT
EA19930313–17:12:28–Har	38.55	19.42	15	5.7	144	40	–084	140	050	NF	Harvard CMT
EA19930314–08:12:20–Har	38.74	19.65	15	4.9	301	45	–090	121	031	NF	Harvard CMT
EA19930316–11:59:29–Har	38.61	19.18	15	5.3	127	38	–114	141	051	NF	Harvard CMT
EA19930322–20:51:39–Har	38.59	19.43	15	5.0	315	45	–090	135	045	NF	Harvard CMT
EA19930323–00:59:37–Har	38.39	19.85	16	5.2	313	45	–090	133	043	NF	Harvard CMT
EA19961102–13:50:38–Har	38.94	19.13	15	5.3	153	20	–068	142	052	NF	Harvard CMT
EA20010525–22:18:25–Har	40.07	18.21	15	5.2	303	36	–128	146	056	NF	Harvard CMT
EA20060702–23:45:10–Har	39.28	19.09	12	4.7	329	29	–093	151	061	NF	Harvard CMT
<i>Western Afar (box 2)</i>											
EA19711113–15:47:44–Shu	39.70	11.00	14	5.3	174	50	–090	174	084	NF	Shudofsky 1985
EA19770708–06:23:08–Har	39.98	10.42	15	5.3	310	66	–171	173	083	SS	Harvard CMT
EA19890413–12:17:26–Har	39.48	12.94	15	5.4	168	39	–070	156	066	NF	Harvard CMT
EA19930506–20:36:03–Har	40.14	14.52	15	5.2	337	45	–090	157	067	NF	Harvard CMT
EA19930921–19:11:46–Har	40.05	11.19	15	5.7	299	38	–159	156	066	U	Harvard CMT
EA20020808–21:17:18–Har	39.90	13.74	15	4.9	351	45	–090	171	081	NF	Harvard CMT
EA20020810–15:56:09–Har	39.90	13.79	15	5.7	164	24	–068	152	062	NF	Harvard CMT
EA20021201–11:18:38–Har	39.91	12.24	15	5.1	003	23	–104	011	101	NF	Harvard CMT
EA20041022–12:00:14–Har	40.25	14.41	12	5.4	170	40	–071	159	069	NF	Harvard CMT
EA20050920–21:23:40–Har	40.47	12.76	12	5.4	251	77	–012	028	118	SS	Harvard CMT
EA20050921–14:57:28–Har	40.49	12.74	12	5.0	250	71	–014	027	117	SS	Harvard CMT
EA20050922–03:12:36–Har	40.47	12.69	12	5.2	248	55	–031	033	123	NS	Harvard CMT
EA20050922–13:58:47–Har	40.51	12.80	12	5.2	311	46	–107	143	053	NF	Harvard CMT
EA20050922–19:51:56–Har	40.41	12.81	12	5.1	296	42	–138	144	054	NF	Harvard CMT
EA20050924–05:15:36–Har	40.53	12.76	12	5.2	170	44	–080	163	073	NF	Harvard CMT
EA20050924–06:58:32–Har	40.55	12.81	12	5.3	173	39	–068	159	069	NF	Harvard CMT
EA20050924–07:36:13–Har	40.50	12.82	12	5.2	173	45	–065	156	066	NF	Harvard CMT
EA20050924–08:20:51–Har	40.46	12.84	12	5.1	307	52	–131	154	064	NF	Harvard CMT
EA20050924–19:24:06–Har	40.68	12.55	12	5.6	122	68	–166	165	075	SS	Harvard CMT
EA20050925–00:37:31–Har	40.60	12.62	12	5.1	174	44	–068	160	070	NF	Harvard CMT
EA20050925–01:11:03–Har	40.60	12.54	12	4.9	168	47	–062	149	059	NF	Harvard CMT
EA20050925–08:18:43–Har	40.60	12.45	12	5.0	341	36	–062	145	055	NF	Harvard CMT
EA20050925–10:02:17–Har	40.58	12.53	12	5.0	144	43	–084	140	050	NF	Harvard CMT
EA20050925–11:20:06–Har	40.65	12.54	12	5.1	333	42	–083	148	058	NF	Harvard CMT
EA20050926–13:28:32–Har	40.31	12.42	12	5.2	006	39	–059	167	077	NF	Harvard CMT
EA20050926–20:30:02–Har	40.58	12.61	12	5.1	323	45	–111	157	067	NF	Harvard CMT
EA20050926–21:25:04–Har	40.54	12.60	12	5.0	327	42	–104	156	066	NF	Harvard CMT
EA20050928–16:31:37–Har	40.62	12.53	12	5.1	341	36	–074	151	061	NF	Harvard CMT
EA20051002–23:24:46–Har	40.60	12.51	12	4.9	342	41	–082	156	066	NF	Harvard CMT
EA20060410–13:36:49–Har	40.26	14.87	20	4.9	172	29	–075	163	073	NF	Harvard CMT
EA20071002–09:06:32–Har	40.99	13.55	14	5.0	010	65	–021	149	059	SS	Harvard CMT
<i>Central Afar (box 3)</i>											
EA19690329–09:15:54–Fos	41.21	11.91	9	6.2	325	74	–020	103	013	SS	Foster & J. 1998
EA19690329–11:04:00–Keb	41.40	11.90	5	5.6	072	83	174	117	027	SS	Kebede & K. 1991
EA19690329–13:08:00–Keb	41.30	11.90		5.1	103	68	176	149	059	SS	Kebede & K. 1991
EA19690405–02:18:30–Fos	41.35	12.00	5	6.2	320	66	–051	108	018	NS	Foster & J. 1998
EA19690406–16:51:00–Keb	41.40	12.00	5	5.1	088	56	179	133	043	U	Kebede & K. 1991
EA19690505–02:45:00–Keb	41.30	12.10		4.9	072	66	176	119	029	SS	Kebede & K. 1991
EA19781107–17:05:59–Har	42.67	11.64	15	5.9	064	65	–178	109	019	SS	Harvard CMT
EA19781108–05:08:02–Har	42.67	11.66	15	5.8	150	80	–009	106	016	SS	Harvard CMT
EA19781221–04:03:59–Har	42.91	11.79	15	5.7	155	76	–012	112	022	SS	Harvard CMT
EA19830928–21:02:40–Har	43.01	11.71	15	5.3	232	67	174	098	008	SS	Harvard CMT
EA19830930–18:58:18–Har	43.47	11.83	37	5.7	058	67	–168	100	010	SS	Harvard CMT
EA19831019–04:45:59–Har	43.17	11.91	10	5.4	232	74	–165	095	005	SS	Harvard CMT
EA19850604–02:43:46–Har	42.93	11.31	10	5.1	149	54	–027	113	023	NS	Harvard CMT
EA19890820–11:17:08–Har	42.04	11.99	16	6.5	301	45	–090	121	031	NF	Harvard CMT
EA19890820–11:46:34–Har	41.90	11.86	15	6.1	288	38	–109	121	031	NF	Harvard CMT
EA19890820–18:39:45–Har	41.42	11.32	15	5.7	294	45	–090	114	024	NF	Harvard CMT
EA19890820–19:26:07–Har	41.91	12.40	15	6.1	285	34	–092	106	016	NF	Harvard CMT
EA19890821–01:09:16–Har	41.88	12.19	15	6.4	281	45	–101	109	019	NF	Harvard CMT
EA19890821–05:03:13–Har	41.56	12.17	15	6.1	290	41	–077	101	011	NF	Harvard CMT
EA19890821–05:05:54–Har	41.71	11.92	15	5.8	296	45	–090	116	026	NF	Harvard CMT
EA19890821–07:07:36–Har	41.18	11.10	15	5.3	296	32	–078	109	019	NF	Harvard CMT
EA19920305–08:55:13–Har	42.98	11.75	16	6.2	324	74	003	099	009	SS	Harvard CMT
EA19930316–22:59:48–Har	41.82	11.49	15	5.6	308	37	–076	119	029	NF	Harvard CMT

Table 1 (continued)

Date-time group Event	Location			Data				SH		Stress	Source
	Long	Lat	Depth	M <sub>W</sub>	Strike	Dip	Slip	Max	Min	Reg.	
<i>Central Afar (box 3)</i>											
EA19940411–11:20:26–Har	43.15	11.82	15	5.9	318	78	–002	093	003	SS	Harvard CMT
EA19940424–02:57:18–Har	43.03	11.85	15	5.6	120	34	–067	107	017	NF	Harvard CMT
EA19970308–23:29:09–Har	43.64	11.90	15	5.3	077	47	–143	108	018	NS	Harvard CMT
EA19970309–17:40:23–Har	43.75	12.04	15	5.5	315	58	–024	096	006	SS	Harvard CMT
EA20011102–16:23:50–Har	43.41	11.72	15	5.1	053	63	179	098	008	SS	Harvard CMT
EA20020809–22:08:49–Har	43.85	12.08	15	5.2	323	52	–037	111	021	NS	Harvard CMT
EA20020810–09:45:47–Har	43.88	12.13	15	4.9	323	45	–090	143	053	NF	Harvard CMT
EA20040103–23:17:55–Har	43.28	11.84	12	5.2	307	51	–038	095	005	NS	Harvard CMT
EA20040104–00:09:49–Har	43.33	11.81	12	5.3	076	48	–122	098	008	NF	Harvard CMT
EA20061221–09:07:46–Har	43.82	11.96	15	5.0	270	40	–126	112	022	NF	Harvard CMT
<i>Gulf of Aden (box 4)</i>											
EA19790924–23:41:45–Har	48.81	13.46	15	5.2	268	45	–090	089	179	NF	Harvard CMT
EA19821208–06:19:45–Har	46.13	12.03	14	5.6	105	39	–093	107	017	NF	Harvard CMT
EA19860523–09:51:28–Har	48.14	12.94	15	5.7	314	44	–062	116	026	NF	Harvard CMT
EA19891124–07:22:30–Har	48.55	12.83	15	5.5	041	67	–168	083	173	SS	Harvard CMT
EA19910511–15:26:34–Har	47.48	12.84	15	5.4	308	82	–008	084	174	SS	Harvard CMT
EA19910512–16:12:42–Har	47.07	12.67	15	5.5	275	45	–090	095	005	NF	Harvard CMT
EA19930108–17:31:12–Har	49.33	13.26	15	5.5	231	30	–134	075	165	NF	Harvard CMT
EA19981123–19:16:49–Har	47.54	12.43	15	5.4	305	53	–033	090	000	NS	Harvard CMT
EA20000210–01:35:04–Har	45.95	12.01	15	5.1	270	45	–090	090	000	NF	Harvard CMT
EA20000214–06:38:31–Har	46.30	11.89	15	5.4	120	31	–052	099	009	NF	Harvard CMT
EA20030126–20:22:04–Har	48.04	12.67	15	5.1	287	67	014	058	148	SS	Harvard CMT
EA20060430–03:08:46–Har	49.10	12.81	19	5.0	221	48	–166	082	172	U	Harvard CMT
EA20061207–11:58:25–Har	46.29	12.15	22	4.9	188	76	007	142	052	SS	Harvard CMT
EA20070802–13:37:30–Har	47.51	12.62	16	5.7	226	57	–164	086	176	SS	Harvard CMT
EA20070831–21:09:47–Har	47.97	12.83	25	5.1	209	42	174	076	166	U	Harvard CMT
<i>Main Ethiopian Rift (box 5)</i>											
EA19831202–23:08:46–Har	38.59	7.41	15	5.3	342	40	–101	169	079	NF	Harvard CMT
EA19850820–05:46:06–Har	35.96	5.72	10	5.4	258	31	–045	054	144	NF	Harvard CMT
EA19871007–22:29:29–Har	37.31	6.54	15	5.3	216	20	–079	030	120	NF	Harvard CMT
EA19871025–16:46:23–Har	36.40	5.77	15	6.2	232	38	–051	029	119	NF	Harvard CMT
EA19871028–08:58:36–Har	36.65	5.92	15	6.0	211	45	–078	022	112	NF	Harvard CMT
EA19890608–06:24:18–Har	38.16	7.35	15	4.9	200	45	–090	020	110	NF	Harvard CMT
EA19930213–02:25:50–Har	39.06	7.75	15	5.3	090	74	010	043	133	SS	Harvard CMT
<i>Gregory Rift-stand alone</i>											
EA19280106–19:31:00–Dos	36.20	0.20	7	6.7	348	77	–006	123	033	SS	Doser & Y. 1991
EA19720213–10:02:42–Shu	34.10	–4.50	6	5.3	340	62	–061	135	045	NF	Shudofsky 1985
EA19980500–00:00:00–lbs	36.30	–1.70	5	5.2	205	65	–081	015	105	NF	lbs-v.-S. & al. 2001
EA20020518–15:15:14–Har	33.64	–2.98	15	5.5	150	76	010	104	014	SS	Harvard CMT
EA20021223–02:50:42–Har	34.69	–1.78	15	5.2	225	59	175	091	001	SS	Harvard CMT
<i>Gregory Rift. Lake Natron (box 6a)</i>											
EA19640507–05:45:00–Nyb	34.92	–3.90	34	6.4	283	89	044	057	147	U	Nyblade & L. 1995
EA19900405–19:20:49–Har	36.05	–3.05	15	5.1	352	45	–090	172	082	NF	Harvard CMT
EA19900515–15:21:28–Har	35.77	–3.43	15	5.4	332	29	–106	162	072	NF	Harvard CMT
EA19900515–16:24:25–Har	35.40	–3.12	15	5.5	059	43	–132	086	176	NF	Harvard CMT
EA19910222–22:06:17–Har	35.94	–3.94	15	5.2	182	45	–104	012	102	NF	Harvard CMT
EA19940212–16:37:33–Bra	35.67	–3.88	34	4.5	316	68	–077	120	030	NF	Brazier & al. 2005
EA19940720–11:32:03–Bra	35.59	–4.25	21	4.5	301	64	–011	078	168	SS	Brazier & al. 2005
EA19941127–04:20:53–Bra	35.83	–4.08	11	4.0	093	69	–022	052	142	SS	Brazier & al. 2005
EA20070715–11:24:24–Har	35.58	–2.82	18	5.3	235	47	–124	078	168	NF	Harvard CMT
EA20070715–20:42:15–Har	35.88	–2.66	12	5.4	247	42	–079	059	149	NF	Harvard CMT
EA20070717–14:10:47–Har	35.93	–2.72	12	5.9	236	40	–094	059	149	NF	Harvard CMT
EA20070717–18:27:55–Har	35.91	–2.68	12	5.3	239	34	–089	058	148	NF	Harvard CMT
EA20070718–17:25:56–Har	35.80	–2.73	12	5.2	245	43	–099	071	161	NF	Harvard CMT
EA20070726–18:54:41–Har	35.74	–2.79	17	5.2	233	45	–116	070	160	NF	Harvard CMT
EA20070818–07:44:04–Har	35.84	–2.72	12	5.2	260	45	–082	074	164	NF	Harvard CMT
EA20070820–02:56:51–Har	35.95	–2.75	12	5.4	237	34	–099	063	153	NF	Harvard CMT
EA20070908–14:15:35–Har	36.11	–2.59	12	4.9	213	36	–092	034	124	NF	Harvard CMT
EA20071223–13:45:30–Har	36.10	–2.75	12	5.2	106	36	–100	112	022	NF	Harvard CMT
<i>Gregory Rift. Manyara–Dodoma (box 6b)</i>											
EA19771215–23:20:57–Har	34.70	–4.84	15	5.7	151	31	–064	135	045	NF	Harvard CMT
EA19940129–00:23:33–Bra	35.92	–5.03	9	4.1	162	43	–071	150	060	NF	Brazier & al. 2005
EA19940817–03:23:32–Bra	35.59	–4.48	15	3.7	335	35	–010	114	024	U	Brazier & al. 2005
EA19961220–03:53:25–Har	35.96	–5.18	15	5.1	229	57	–010	007	097	SS	Harvard CMT
EA19961221–08:34:06–Bar	35.80	–5.30	25	5.5	033	49	–037	001	091	NS	Barth & al. 2007
EA19970223–01:39:35–Bar	34.80	–5.30	10	4.9	190	14	155	067	157	U	Barth & al. 2007
EA20010325–18:54:14–Bar	35.90	–5.70	33	4.5	202	17	–053	003	093	NF	Barth & al. 2007
EA20030614–03:10:25–Har	35.97	–5.71	15	5.0	340	26	–112	171	081	NF	Harvard CMT
EA20080306–07:35:39–Har	35.91	–5.44	16	5.4	145	80	–170	009	099	SS	Harvard CMT

(continued on next page)

Table 1 (continued)

Date–time group Event	Location			Data				SH		Stress Reg.	Source
	Long	Lat	Depth	$M_W$	Strike	Dip	Slip	Max	Min		
<i>Indian Coast (box 7)</i>											
EA19671014–23:29:14–Shu	38.20	– 3.30	10	5.2	142	70	– 125	174	084	NS	Shudofsky 1985
EA19900313–23:05:37–Har	40.48	– 3.87	15	5.5	323	46	– 121	163	073	NF	Harvard CMT
EA19951208–23:40:52–Bar	38.80	– 4.60	18	4.9	102	43	– 128	126	036	NF	Barth & al. 2007
EA19990406–04:16:47–Bar	39.40	– 8.50	14	5.0	223	31	– 050	021	111	NF	Barth & al. 2007
EA20050115–05:13:15–Har	39.19	– 6.12	32	5.0	159	45	– 116	176	086	NF	Harvard CMT
EA20071208–19:55:24–Har	37.49	– 7.44	12	5.6	214	28	– 104	042	132	NF	Harvard CMT
EA20071223–12:56:16–Har	39.45	– 4.08	13	4.9	299	42	– 082	114	024	NF	Harvard CMT
<i>Mozambique Channel (box 8)</i>											
EA19750215–06:16:26–Gri	41.50	– 16.50	25	5.2	350	20	– 075	162	072	NF	Grimison & C. 1988
EA19791106–04:54:15–Har	41.61	– 12.01	15	5.2	318	35	– 135	164	074	NF	Harvard CMT
EA19820429–20:20:27–Har	41.57	– 9.97	15	5.1	356	45	– 090	176	086	NF	Harvard CMT
EA19830903–10:21:28–Har	41.04	– 15.35	15	5.0	340	45	– 090	160	070	NF	Harvard CMT
EA19850514–13:25:06–Har	41.54	– 10.27	10	6.0	178	43	– 070	165	075	NF	Harvard CMT
EA19850514–18:11:17–Har	41.36	– 10.26	14	6.3	170	34	– 089	169	079	NF	Harvard CMT
EA19850530–08:32:25–Har	41.62	– 10.25	10	5.3	148	38	– 104	157	067	NF	Harvard CMT
EA19850628–07:32:27–Har	41.55	– 10.30	10	5.6	346	44	– 093	168	078	NF	Harvard CMT
EA19950720–05:08:28–Bar	41.50	– 12.40	18	5.0	174	48	160	046	136	TS	Barth & al. 2007
EA19950810–00:41:09–Har	41.41	– 15.51	15	5.2	332	41	– 115	168	078	NF	Harvard CMT
EA20000114–03:32:44–Bar	41.90	– 16.00	6	4.8	347	14	049	099	009	TF	Barth & al. 2007
EA20020716–14:50:21–Har	41.01	– 11.71	15	5.2	195	34	– 050	173	083	NF	Harvard CMT
EA20050104–19:58:03–Har	41.39	– 10.35	17	5.0	177	39	– 058	158	068	NF	Harvard CMT
EA20060624–10:22:14–Har	41.67	– 17.50	18	4.8	332	38	– 115	168	078	NF	Harvard CMT
EA20060625–04:51:59–Har	41.77	– 17.36	15	4.9	188	46	– 074	177	087	NF	Harvard CMT
EA20060917–07:30:14–Har	41.76	– 17.56	12	5.1	003	37	– 096	007	097	NF	Harvard CMT
EA20060917–13:24:57–Har	41.71	– 17.54	20	5.1	347	38	– 095	170	080	NF	Harvard CMT
EA20060924–22:56:24–Har	41.78	– 17.59	12	5.6	350	40	– 091	171	081	NF	Harvard CMT
EA20070618–23:51:13–Har	41.89	– 12.40	14	5.0	116	36	– 066	102	012	NF	Harvard CMT
EA20070916–14:01:53–Har	42.00	– 11.74	42	5.0	262	36	– 101	089	179	NF	Harvard CMT
EA20080121–02:49:14–Har	41.44	– 10.36	18	5.2	165	34	– 090	165	075	NF	Harvard CMT
EA20080121–15:28:39–Har	41.43	– 10.43	20	5.1	308	36	– 151	162	072	U	Harvard CMT
EA20080827–06:46:19–Har	41.37	– 10.69	10	5.7	305	32	– 142	153	63	NF	Harvard CMT
<i>Madagascar (box 9)</i>											
EA19750404–17:41:16–Shu	45.13	– 21.24	11	5.6	074	85	040	027	117	U	Shudofsky 1985
EA19830131–17:37:53–Har	44.39	– 23.00	15	5.1	326	45	– 090	146	056	NF	Harvard CMT
EA19831227–00:39:10–Har	44.96	– 17.88	34	5.1	158	35	– 098	163	073	NF	Harvard CMT
EA19851004–15:17:16–Har	48.62	– 18.08	10	5.5	147	32	– 115	161	071	NF	Harvard CMT
EA19910421–23:12:29–Har	46.42	– 18.51	15	5.5	327	44	– 128	170	080	NF	Harvard CMT
EA19921114–05:54:55–Har	45.54	– 23.01	15	5.0	350	45	– 090	170	080	NF	Harvard CMT
EA19980922–19:27:35–Bar	45.40	– 20.10	33	5.0	078	30	– 035	048	138	NF	Barth & al. 2007
<i>South-Sudan (box 10)</i>											
EA19900520–02:22:08–Har	32.29	5.32	15	7.1	224	67	176	090	000	SS	Harvard CMT
EA19900524–19:34:54–Har	31.64	5.93	15	6.5	236	39	– 104	065	155	NF	Harvard CMT
EA19900524–20:00:22–Har	31.67	5.70	15	7.1	232	43	– 131	077	167	NF	Harvard CMT
EA19900709–15:11:28–Har	31.60	5.83	15	6.3	028	44	– 149	062	152	NS	Harvard CMT
EA19900728–16:46:12–Har	32.05	6.00	15	5.3	277	45	– 090	097	007	NF	Harvard CMT
EA19900907–00:12:24–Har	31.56	5.10	15	5.5	044	43	– 147	077	167	NS	Harvard CMT
EA19910329–09:06:21–Har	31.84	5.43	15	5.4	130	15	– 051	109	019	NF	Harvard CMT
<i>Albertine Graben–Rwenzori (box 11)</i>											
EA19660320–01:42:52–Fos	29.90	0.81	6	7.0	033	42	– 100	040	130	NF	Foster & J. 1998
EA19660321–01:30:38–Shu	29.60	0.80	7	5.1	040	60	– 102	052	142	NF	Shudofsky 1985
EA19660517–07:03:33–Fos	29.95	0.76	6	5.8	003	53	– 092	004	094	NF	Foster & J. 1998
EA19661005–08:34:40–Shu	29.90	0.00	23	5.2	156	54	– 116	176	086	NF	Shudofsky 1985
EA19740425–00:03:47–Shu	30.10	1.10	10	5.0	009	40	– 087	007	097	NF	Shudofsky 1985
EA19900904–01:48:08–Har	29.42	– 0.12	15	5.3	229	77	006	003	093	SS	Harvard CMT
EA19911009–17:22:08–Har	31.18	2.21	15	5.6	260	56	– 041	048	138	NS	Harvard CMT
EA19940205–23:34:14–Har	29.85	0.50	15	6.2	203	25	– 057	005	095	NF	Harvard CMT
EA19960324–08:24:32–Har	29.93	0.27	15	5.3	179	24	– 094	001	091	NF	Harvard CMT
EA19980815–17:29:19–Bar	30.00	0.70	10	4.5	013	41	– 138	042	132	NF	Barth & al. 2007
EA20001023–12:02:15–Bar	30.70	1.50	25	4.8	052	48	– 037	020	110	NF	Barth & al. 2007
EA20010131–19:15:29–Bar	30.20	0.60	33	4.7	032	40	– 179	077	167	U	Barth & al. 2007
EA20010629–23:40:08–Har	29.97	0.29	15	5.2	017	33	– 060	179	089	NF	Harvard CMT
EA20020104–13:02:21–Bar	29.80	– 0.20	10	5.2	090	38	– 032	058	148	NS	Barth & al. 2007
EA20060427–04:18:32–Har	29.98	0.46	19	5.2	189	32	– 086	007	097	NF	Harvard CMT
EA20060529–15:30:36–Har	29.96	0.21	32	4.9	180	51	– 135	029	119	NF	Harvard CMT
EA20070219–02:33:46–Har	30.65	1.72	29	5.6	160	53	– 153	016	106	NS	Harvard CMT
EA20070615–18:49:56–Har	30.71	1.75	24	5.8	059	56	– 034	024	114	NS	Harvard CMT
<i>Kivu Rift (box 12)</i>											
EA19540703–00:32:57–De	29.07	– 3.24		5.5	009	58	– 145	044	134	NS	De Breae. 1956
EA19770106–18:33:46–Har	28.39	– 2.31	14	5.1	241	45	– 090	061	151	NF	Harvard CMT
EA19800109–14:50:10–Har	27.63	– 2.69	15	5.2	045	48	– 142	076	166	NF	Harvard CMT

Table 1 (continued)

Date-time group Event	Location			Data				SH		Stress	Source
	Long	Lat	Depth	$M_W$	Strike	Dip	Slip	Max	Min	Reg.	
<i>Kivu Rift (box 12)</i>											
EA19810730–16:46:19–Har	28.13	– 2.43	15	5.1	235	45	–090	055	145	NF	Harvard CMT
EA19850628–22:46:22–Har	29.01	– 2.31	10	4.9	211	45	–090	031	121	NF	Harvard CMT
EA19950429–11:50:54–Bar	28.60	– 1.30	6	5.4	229	22	–055	030	120	NF	Barth & al. 2007
EA20000302–02:44:56–Bar	28.40	– 2.20	6	4.7	009	42	–133	034	124	NF	Barth & al. 2007
EA20000302–04:29:50–Bar	28.20	– 2.40	25	4.7	033	75	–103	054	144	NF	Barth & al. 2007
EA20000303–05:03:22–Bar	28.20	– 2.40	33	4.6	037	83	–137	079	169	U	Barth & al. 2007
EA20020117–20:01:31–Bar	29.20	– 1.70	25	5.0	016	71	–082	004	094	NF	Barth & al. 2007
EA20020119–17:09:32–Bar	29.60	– 1.90	33	4.8	009	80	–088	003	093	U	Barth & al. 2007
EA20020120–00:14:48–Har	29.20	– 1.67	15	5.1	039	49	–042	009	099	NF	Harvard CMT
EA20020121–04:39:25–Har	29.04	– 1.78	15	5.1	018	26	–128	038	128	NF	Harvard CMT
EA20020122–15:32:09–Har	28.86	– 1.51	15	5.2	233	26	–043	029	119	NF	Harvard CMT
EA20021024–06:08:43–Har	28.68	– 1.86	15	6.2	210	42	–075	020	110	NF	Harvard CMT
EA20021024–07:12:20–Bar	28.90	– 1.90	33	5.2	033	37	–146	064	154	NF	Barth & al. 2007
EA20030320–06:15:23–Har	29.57	– 3.04	15	5.2	017	45	–023	160	070	NS	Harvard CMT
EA20030805–18:56:54–Har	29.42	– 0.81	15	5.2	330	34	–155	005	095	U	Harvard CMT
EA20080203–07:34:15–Har	28.82	– 2.38	12	5.9	179	35	–096	002	092	NF	Harvard CMT
EA20080203–10:56:11–Har	28.91	– 2.54	18	5.0	010	42	–068	175	085	NF	Harvard CMT
EA20080214–02:07:48–Har	28.84	– 2.37	12	5.3	005	45	–084	001	091	NF	Harvard CMT
<i>North-Tanganyika (box 13)</i>											
EA19750326–03:40:48–Shu	30.10	– 5.30	16	5.5	354	51	–112	011	101	NF	Shudofsky 1985
EA19770706–08:48:37–Shu	29.60	– 6.30	14	5.3	168	63	–077	154	064	NF	Shudofsky 1985
EA19820703–23:21:23–Har	29.01	– 3.65	15	5.3	328	50	–136	177	087	NF	Harvard CMT
EA19860629–21:48:10–Har	29.46	– 4.96	29	5.8	318	22	–148	167	077	U	Harvard CMT
EA19940930–01:36:53–Bra	29.89	– 5.92	11	4.5	335	36	–010	114	024	U	Brazier & al. 2005
EA19941225–04:25:35–Bra	30.58	– 5.17	29	4.2	215	55	–065	016	106	NF	Brazier & al. 2005
EA19980328–22:00:03–Har	29.17	– 5.92	15	5.3	257	45	–016	027	117	U	Harvard CMT
EA200001215–10:01:23–Bar	29.40	– 5.50	33	4.7	012	52	–040	161	071	NS	Barth & al. 2007
EA20030410–16:03:59–Har	29.06	– 5.22	15	5.1	061	46	–049	035	125	NF	Harvard CMT
EA20051205–12:20:04–Har	29.60	– 6.23	18	6.8	149	50	–122	171	081	NF	Harvard CMT
EA20051206–05:53:13–Har	29.53	– 6.16	18	5.2	019	40	–058	180	090	NF	Harvard CMT
EA20051208–03:16:37–Har	29.61	– 6.06	22	5.0	190	44	–107	022	112	NF	Harvard CMT
EA20051208–11:51:39–Har	29.48	– 6.12	35	5.1	184	39	–090	004	094	NF	Harvard CMT
EA20051209–23:30:28–Har	29.67	– 6.19	16	5.5	033	39	–054	011	101	NF	Harvard CMT
EA20060109–20:59:41–Har	29.54	– 5.87	27	5.3	248	51	–022	030	120	NS	Harvard CMT
EA20070328–21:17:14–Har	29.70	– 6.36	14	5.8	025	61	–026	166	076	SS	Harvard CMT
<i>South-Tanganyika (box 14)</i>											
EA19941002–02:25:32–Bra	30.82	– 7.85	35	6.5	189	36	–073	179	089	NF	Brazier & al. 2005
EA19941112–12:17:57–Bra	29.55	– 6.94	18	5.3	204	80	–020	161	071	SS	Brazier & al. 2005
EA19941112–20:16:58–Bra	30.14	– 6.65	8	4.7	303	46	–035	091	001	NS	Brazier & al. 2005
EA19970921–18:13:33–Har	30.27	– 7.29	30	5.9	315	36	–133	159	069	NF	Harvard CMT
EA20001002–02:25:38–Har	30.60	– 7.79	40	6.4	172	32	–085	169	079	NF	Harvard CMT
EA20001005–23:08:36–Bar	30.50	– 8.00	25	4.8	161	57	–084	156	066	NF	Barth & al. 2007
EA20001007–01:39:10–Bar	30.70	– 8.00	25	4.7	149	56	–032	114	024	NS	Barth & al. 2007
EA20010713–19:24:02–Bar	30.90	– 6.90	42	4.6	012	12	–110	023	113	NF	Barth & al. 2007
EA20060713–05:36:43–Har	30.25	– 8.33	36	5.0	162	34	–098	167	077	NF	Harvard CMT
<i>Rukwa Rift (box 15)</i>											
EA19840825–20:38:00–Har	32.79	– 7.88	10	5.3	126	42	–122	146	056	NF	Harvard CMT
EA19920905–23:34:52–Fer	32.12	– 8.78	29	2.9	310	23	–87	129	039	NF	Ferd. & A. 2002b
EA19921009–06:53:11–Fer	32.13	– 8.82	29	3.9	308	84	–082	100	010	U	Ferd. & A. 2002b
EA19921013–13:36:39–Fer	32.40	– 8.97	24	3.0	263	23	–137	106	016	NF	Ferd. & A. 2002b
EA19921107–19:51:56–Fer	32.24	– 8.99	26	2.0	242	25	–146	092	002	NF	Ferd. & A. 2002b
EA19930519–20:07:40–Fer	32.37	– 9.14	25	3.0	300	75	–078	100	010	NF	Ferd. & A. 2002b
EA19940818–00:45:53–Har	31.83	– 7.65	25	5.9	317	23	–107	146	056	NF	Harvard CMT
EA19940905–04:08:54–Bra	31.70	– 7.50	15	4.1	318	36	–063	122	032	NF	Brazier & al. 2005
EA19990507–02:10:45–Bar	31.60	– 7.50	25	4.8	305	48	–152	160	070	NS	Barth & al. 2007
EA19990507–14:07:33–Bar	31.70	– 7.50	25	5.2	294	52	–130	141	051	NF	Barth & al. 2007
EA20010918–11:01:02–Bar	31.60	– 7.50	10	4.4	350	37	–169	030	120	U	Barth & al. 2007
EA20020220–19:07:21–Har	31.99	– 8.16	45	5.5	135	42	–079	127	037	NF	Harvard CMT
<i>Mbeya triple junction (box 16)</i>											
EA19920619–16:23:41–Fer	33.17	– 8.89	15	1.7	078	29	–105	087	177	NF	Ferd. & A. 2002b
EA19920625–02:13:13–Fer	33.09	– 8.57	17	1.7	028	16	–110	038	128	NF	Ferd. & A. 2002b
EA19920625–09:14:03–Fer	33.09	– 8.61	17	2.8	026	20	–111	037	127	NF	Ferd. & A. 2002b
EA19920704–13:41:55–Fer	33.22	– 8.80	18	2.7	320	10	–033	114	024	U	Ferd. & A. 2002b
EA19920715–08:58:31–Fer	33.10	– 8.59	16	2.1	044	25	–093	045	135	NF	Ferd. & A. 2002b
EA19920817–01:55:56–Fer	33.18	– 8.65	21	2.3	055	23	–091	056	146	NF	Ferd. & A. 2002b
EA19920909–08:59:10–Fer	33.19	– 8.80	16	2.0	072	14	–095	074	164	NF	Ferd. & A. 2002b
EA19920926–01:26:54–Fer	33.24	– 8.85	21	1.5	337	14	–020	122	032	U	Ferd. & A. 2002b
EA19921001–06:24:34–Fer	33.34	– 8.85	20	2.3	028	24	–160	064	154	U	Ferd. & A. 2002b
EA19921108–22:02:58–Fer	33.17	– 8.61	16	2.2	340	15	–171	020	110	U	Ferd. & A. 2002b
EA19921112–12:50:28–Fer	33.13	– 8.90	18	2.6	031	27	–155	064	154	U	Ferd. & A. 2002b

(continued on next page)

Table 1 (continued)

Date–time group Event	Location			Data				SH		Stress Reg.	Source
	Long	Lat	Depth	$M_W$	Strike	Dip	Slip	Max	Min		
<i>Mbeya triple junction (box 16)</i>											
EA19921114–05:43:21–Fer	33.21	– 8.90	17	1.9	052	16	– 136	076	166	NF	Ferd. & A. 2002b
EA19921115–09:38:16–Fer	33.17	– 8.84	18	1.6	305	17	– 052	106	016	NF	Ferd. & A. 2002b
EA19930722–09:10:43–Fer	33.05	– 8.62	26	2.5	063	52	– 024	025	115	NS	Ferd. & A. 2002b
EA19930829–14:18:48–Fer	33.21	– 8.81	23	2.4	073	37	000	027	117	U	Ferd. & A. 2002b
EA19940109–12:24:44–Fer	33.18	– 8.72	10	4.0	197	19	083	110	020	TF	Ferd. & A. 2002b
EA19940417–17:58:54–Fer	33.24	– 8.82	17	1.8	125	24	009	076	166	U	Ferd. & A. 2002b
EA19940701–06:58:51–Fer	33.22	– 8.77	20	2.3	135	39	031	078	168	TS	Ferd. & A. 2002b
EA19941116–01:08:05–Bra	33.51	– 9.42	7	4.5	143	88	– 005	098	008	SS	Brazier & al. 2005
<i>Malawi Rift (box 17)</i>											
EA19540117–17:39:38–De	36.00	– 16.50		6.7	197	068	164	070	160	U	De Breae. 1956
EA19660506–02:36:54–Shu	34.60	– 15.70	17	5.1	227	50	– 056	024	114	NF	Shudofsky 1985
EA19780108–06:31:55–Har	34.45	– 11.76	15	4.9	338	45	– 090	158	068	NF	Harvard CMT
EA19890309–02:37:06–Har	34.33	– 13.44	15	5.6	128	23	– 118	142	052	NF	Harvard CMT
EA19890310–21:49:54–Har	34.34	– 13.40	15	6.3	142	17	– 102	149	059	NF	Harvard CMT
EA19890905–20:49:41–Har	34.46	– 11.80	20	5.4	063	52	149	118	028	TS	Harvard CMT
EA19960830–06:58:45–Bar	34.10	– 15.40	10	4.5	021	27	– 046	178	088	NF	Barth & al. 2007
EA19980824–12:12:11–Bar	34.90	– 13.80	10	4.5	339	33	– 129	001	091	NF	Barth & al. 2007
EA19990901–04:07:57–Bar	34.20	– 10.10	10	4.7	147	16	– 144	174	084	U	Barth & al. 2007
EA20000104–00:25:09–Bar	36.10	– 16.10	25	4.8	194	26	– 070	004	094	NF	Barth & al. 2007
EA20020831–22:52:39–Har	34.28	– 10.22	15	5.2	136	25	– 109	146	056	NF	Harvard CMT
EA20040314–14:08:02–Har	34.35	– 10.08	29	4.8	162	44	– 117	180	090	NF	Harvard CMT
EA20040821–20:11:50–Har	34.44	– 10.60	12	4.7	346	61	– 017	125	035	SS	Harvard CMT
<i>Central Mozambique (box 18)</i>											
EA19901103–00:31:37–Har	33.26	– 21.51	15	5.1	345	35	– 111	177	087	NF	Harvard CMT
EA19910724–13:54:52–Har	34.62	– 18.30	25	5.1	180	45	– 090	000	090	NF	Harvard CMT
EA20060222–22:19:15–Har	33.33	– 21.20	12	7.0	325	27	– 114	159	069	NF	Harvard CMT
EA20060223–01:23:43–Har	33.18	– 21.33	12	5.7	354	32	– 089	173	083	NF	Harvard CMT
EA20060223–21:32:07–Har	33.34	– 21.01	12	5.1	305	44	– 137	153	063	NF	Harvard CMT
EA20060315–11:52:54–Har	33.35	– 20.93	12	5.1	314	45	– 114	150	060	NF	Harvard CMT
EA20060315–14:19:49–Har	33.36	– 20.98	12	5.6	301	52	– 141	153	063	NS	Harvard CMT
EA20060319–16:23:44–Har	33.37	– 21.29	16	4.8	179	49	– 031	145	055	NS	Harvard CMT
EA20060322–11:35:15–Har	33.15	– 21.25	12	5.2	017	42	– 059	177	087	NF	Harvard CMT
EA20060323–06:14:44–Har	33.38	– 21.29	13	4.8	254	30	– 099	079	169	NF	Harvard CMT
EA20060414–18:41:40–Har	33.57	– 21.27	30	5.2	022	37	– 061	004	094	NF	Harvard CMT
EA20060512–18:12:20–Har	33.38	– 21.25	29	4.9	142	42	– 104	151	061	NF	Harvard CMT
EA20060608–06:17:26–Har	33.59	– 21.61	20	4.8	120	44	– 116	137	047	NF	Harvard CMT
EA20060630–01:07:28–Har	33.15	– 20.89	12	5.0	170	45	– 106	001	091	NF	Harvard CMT
EA20060711–18:48:15–Har	33.14	– 20.94	12	4.9	018	41	– 073	007	097	NF	Harvard CMT
EA20060823–00:53:35–Har	33.33	– 21.09	23	5.0	352	40	– 089	171	081	NF	Harvard CMT
EA20061120–20:16:06–Har	33.12	– 20.88	12	5.1	014	39	– 070	002	092	NF	Harvard CMT
EA20071129–02:59:13–Har	33.12	– 21.03	12	5.2	360	28	– 069	169	079	NF	Harvard CMT
EA20080203–11:12:14–Har	33.02	– 20.98	20	5.1	187	45	– 069	173	083	NF	Harvard CMT
<i>South Africa (box 19)</i>											
EA19690929–20:03:32–Fos	19.52	– 33.09	5	6.4	305	87	003	080	170	SS	Foster & J. 1998
EA19700414–19:08:22–Shu	19.47	– 33.17	10	5.8	154	74	020	106	016	SS	Shudofsky 1985
EA19760701–11:24:05–Fos	25.17	– 29.51	8	5.8	126	64	– 077	112	022	NF	Foster & J. 1998
EA19861005–18:53:27–Har	29.23	– 30.08	15	5.3	168	37	– 090	168	078	NF	Harvard CMT
EA19900926–23:08:29–Har	26.88	– 27.92	28	5.0	011	45	– 061	172	082	NF	Harvard CMT
<i>Luangwa Graben (box 20)</i>											
EA19680515–07:51:17–Fos	26.16	– 15.91	30	5.7	036	34	– 114	050	140	NF	Foster & J. 1998
EA19721218–01:18:53–Shu	28.10	– 16.70	7	5.6	234	58	– 052	026	116	NF	Shudofsky 1985
EA19760919–14:59:43–Fos	32.84	– 11.08	29	5.7	349	42	– 123	010	100	NF	Foster & J. 1998
EA19841026–07:44:35–Har	28.62	– 15.77	10	5.3	215	13	– 071	026	116	NF	Harvard CMT
EA19860718–15:07:56–Har	28.36	– 16.10	15	5.2	238	43	– 084	054	144	NF	Harvard CMT
EA19951112–19:00:10–Bar	31.60	– 13.80	33	5.3	076	36	– 045	050	140	NF	Barth & al. 2007
<i>Mweru Graben (box 21)</i>											
EA19681202–02:33:42–Fos	23.82	– 14.01	11	5.6	035	36	– 081	030	120	NF	Foster & J. 1998
EA19860314–04:16:04–Har	27.17	– 10.53	15	4.9	208	33	– 105	037	127	NF	Harvard CMT
EA19880416–21:17:14–Har	27.43	– 10.17	15	5.1	010	26	– 120	027	117	NF	Harvard CMT
EA19980412–10:49:01–Bar	25.50	– 12.40	33	4.8	340	46	– 141	010	100	NF	Barth & al. 2007
EA20020305–17:07:47–Har	24.62	– 11.79	15	5.1	230	15	– 040	023	113	NF	Harvard CMT
<i>Upemba Graben (box 22)</i>											
EA19830707–20:35:41–Har	27.90	– 7.15	24	5.8	200	41	– 111	034	124	NF	Harvard CMT
EA19840111–18:40:32–Har	27.35	– 6.68	10	5.6	019	62	– 157	058	148	SS	Harvard CMT
EA19920911–03:57:32–Har	26.42	– 5.91	15	6.3	196	38	– 132	040	130	NF	Harvard CMT
EA19920923–14:52:35–Har	26.48	– 5.64	15	5.5	042	50	– 055	018	108	NF	Harvard CMT
EA19951211–17:54:43–Har	26.63	– 6.16	15	5.7	200	27	– 041	174	084	NF	Harvard CMT
EA19970415–19:04:29–Bar	26.40	– 8.70	18	5.0	156	49	– 154	012	102	NS	Barth & al. 2007
EA20001202–04:16:43–Bar	27.80	– 7.30	18	4.7	230	40	– 068	035	125	NF	Barth & al. 2007

Table 1 (continued)

Date-time group Event	Location			Data				SH		Stress	Source
	Long	Lat	Depth	$M_w$	Strike	Dip	Slip	Max	Min	Reg.	
<i>Congo River Basin (box 23)</i>											
EA19740923–19:28:18–Fos	12.83	– 0.28	3	6.1	344	41	086	077	167	TF	Foster & J 1998
EA19760515–08:09:57–Fai	19.35	4.46	23	5.6	250	55	152	123	033	TS	Fairhead & S. 1982
EA19811118–09:17:34–Har	22.81	– 2.46	10	5.5	133	66	– 007	090	000	SS	Harvard CMT
EA19870126–23:11:53–Har	12.95	7.85	15	4.9	174	27	060	100	010	TF	Harvard CMT
EA19950922–08:51:57–Har	19.51	1.12	15	5.3	315	32	116	030	120	TF	Harvard CMT
EA19980305–02:59:52–Har	17.04	1.38	15	5.1	151	33	096	058	148	TF	H. CMT; Ayele 2002
EA19980426–14:16:58–Har	17.40	0.64	15	5.2	165	26	132	053	143	TF	H. CMT; Ayele 2002
EA19990806–17:22:49–Bar	21.60	– 8.60	10	4.6	354	19	073	092	002	TF	Barth & al. 2007
EA20010417–04:39:03–Bar	22.80	– 6.20	33	4.6	287	43	– 037	077	167	NF	Barth & al. 2007
<i>Stand alone</i>											
EA19800503–03:31:02–Har	43.26	10.31	15	5.6	280	40	– 068	085	175	NF	Harvard CMT
EA19800530–08:02:54–Har	43.37	10.05	15	5.3	022	23	– 130	042	132	NF	Harvard CMT
EA19820413–09:13:01–Har	44.60	14.99	10	6.2	134	37	– 095	137	047	NF	Harvard CMT
EA19821229–23:53:12–Har	43.97	14.10	15	5.5	303	43	– 107	135	045	NF	Harvard CMT
EA19930801–00:20:44–Har	31.35	15.37	15	5.5	172	63	– 014	130	040	SS	Harvard CMT
EA19950427–02:32:21–Bar	42.50	– 12.60	25	4.7	283	30	– 024	069	159	U	Barth & al. 2007
EA19960229–07:14:19–Bar	47.00	– 2.40	10	4.9	019	26	042	135	045	TF	Barth & al. 2007
EA20000521–02:58:46–Har	43.34	– 12.48	15	5.2	059	44	171	107	017	U	Harvard CMT
EA20070226–08:48:58–Har	43.19	9.77	12	5.0	266	32	– 079	080	170	NF	Harvard CMT
EA20070623–11:54:60–Har	46.57	– 12.21	49	5.1	352	50	– 011	131	041	U	Harvard CMT

Date-time group: EA (East Africa) followed by date (year–month–day), time (hour–minute–second) and the first 3 letters of the source; Location: Long – Longitude (East), Lat – Latitude (+: North, –: South), Depth (estimated depth in km); Focal mechanism Data:  $M_w$  – moment magnitude, Strike, Dip, Slip of focal plane; Horizontal stress orientations SH: max –  $S_{Hmax}$ , min –  $S_{Hmin}$ ; Source – origin of data.

slip vectors are too similar, data are not independent and the inversion is under-determined and cannot be solved uniquely (Michael, 1984).

For the calculation of confidence regions for the principle stress axes a statistical approach is applied, that inverts different combinations of fault planes, to see which stress tensor is most likely. For this purpose the composition of each dataset is twofold: At first a bootstrap routine is performed that picks  $n$  mechanisms at random from the original  $n$  events. Each dataset then will have some mechanisms repeated two or more times. Thereafter the fault plane is chosen randomly from the two auxiliary planes (Michael, 1987). Thus, at a time 5000 thousand synthetic datasets are compiled by one original set of focal mechanisms and inverted for the orientation of maximum shear stress. The graphical analysis of the resulting stress tensor in an equal-area projection gives confidence regions for the principle stress axes (Fig. 5). The detailed results obtained using SLICK are provided in Table 2a and b (lower row for each box).

For both methods the exact orientations of the horizontal stress axes ( $S_{Hmax}$  and  $S_{Hmin}$ ) are computed with the formula of Lund and Townend (2007). We follow the guidelines and terminology used in the World Stress Map Project, first presented by Zoback (1992a) and regularly updated since then (available online at <http://www.world-stress-map.org>).

In order to express numerically the stress regime, we use the stress regime index  $R'$ , based the value of the stress ratio ( $R$ , Eq. (2)) and the type of stress regime as described in Delvaux et al. (1997) and Delvaux and Sperner (2003). The tectonic stress regime index  $R'$  is defined as:

$$\begin{aligned}
 R' &= R \text{ for normal faulting regimes (NF),} \\
 R' &= (2 - R) \text{ for strike-slip regimes (SS), and} \\
 R' &= (2 + R) \text{ for thrust faulting regimes (TF).}
 \end{aligned}
 \tag{5}$$

It forms a continuous scale ranging from 0 to 1 for normal faulting regimes, from 1 to 2 for strike-slip regimes and from 2 to 3 for thrust faulting regimes.

The quality evaluation of the results was done using the updated quality ranking system of the World Stress Map release 2008 (Heidbach et al., 2010-this issue). It evaluates the azimuthal accuracy of  $S_{Hmax}$  obtained from the formal inversion of  $N$  well-constrained

single-event focal mechanisms with an average misfit angle  $\alpha$  in close geographic proximity (FMF category):

- A – quality ( $S_{Hmax} / S_{Hmin}$  within  $\pm 15^\circ$ ):  $N \geq 15$  and  $\alpha \leq 12^\circ$
- B – quality ( $S_{Hmax} / S_{Hmin}$  within  $\pm 15 - 20^\circ$ ):  $8 \leq N < 15$  and  $12^\circ < \alpha \leq 20^\circ$
- C – quality ( $S_{Hmax} / S_{Hmin}$  within  $\pm 20 - 25^\circ$ ): not defined for FMF category as individual focal mechanism is assessed to C – quality. (6)

To include all of our stress inversion results in the quality ranking we use C-quality for FMF with  $6 \leq N < 8$  or  $\alpha > 20^\circ$ . In addition, we introduce a D-quality ( $S_{Hmax} / S_{Hmin}$  within  $\pm 25 - 40^\circ$ ) for the boxes with only 4 or 5 events, since the calculation results are poorly constrained and very unstable.

A major difference between stress inversion techniques is the handling of the focal mechanism ambiguity concerning determination of the focal and auxiliary planes from the two nodal planes in order to define the actual fault plane. Stress inversion was at first used for slickenside field data and some algorithms need the fault plane to be determined a priori. In most cases this is not possible as further information would be needed to determine which nodal plane was the fault plane. The advantage of both the TENSOR and the SLIK method is that the determination of the fault plane is made during the process and not a priori.

When working with geological fault-slip data, the measured fault population is often inhomogeneous to some degree. As a result, a single stress tensor can generally not model satisfactorily all the observed slips on the fault planes and it is common to use an interactive process of stress tensor calculation and data separation as described in Delvaux and Sperner (2003). This procedure allows often obtaining good quality tensors with an average misfit angle  $\alpha$  lower than  $15^\circ$ . The separation is done by progressively removing the data with the highest misfit angle until all misfit angles fall below  $30 - 40^\circ$ . The same problem might also arise when inverting a population of focal-mechanism data corresponding to a particular volume (box), as the stress field might be heterogeneous within the box. As opposed to the geological fault-slip data for which data separation during inversion

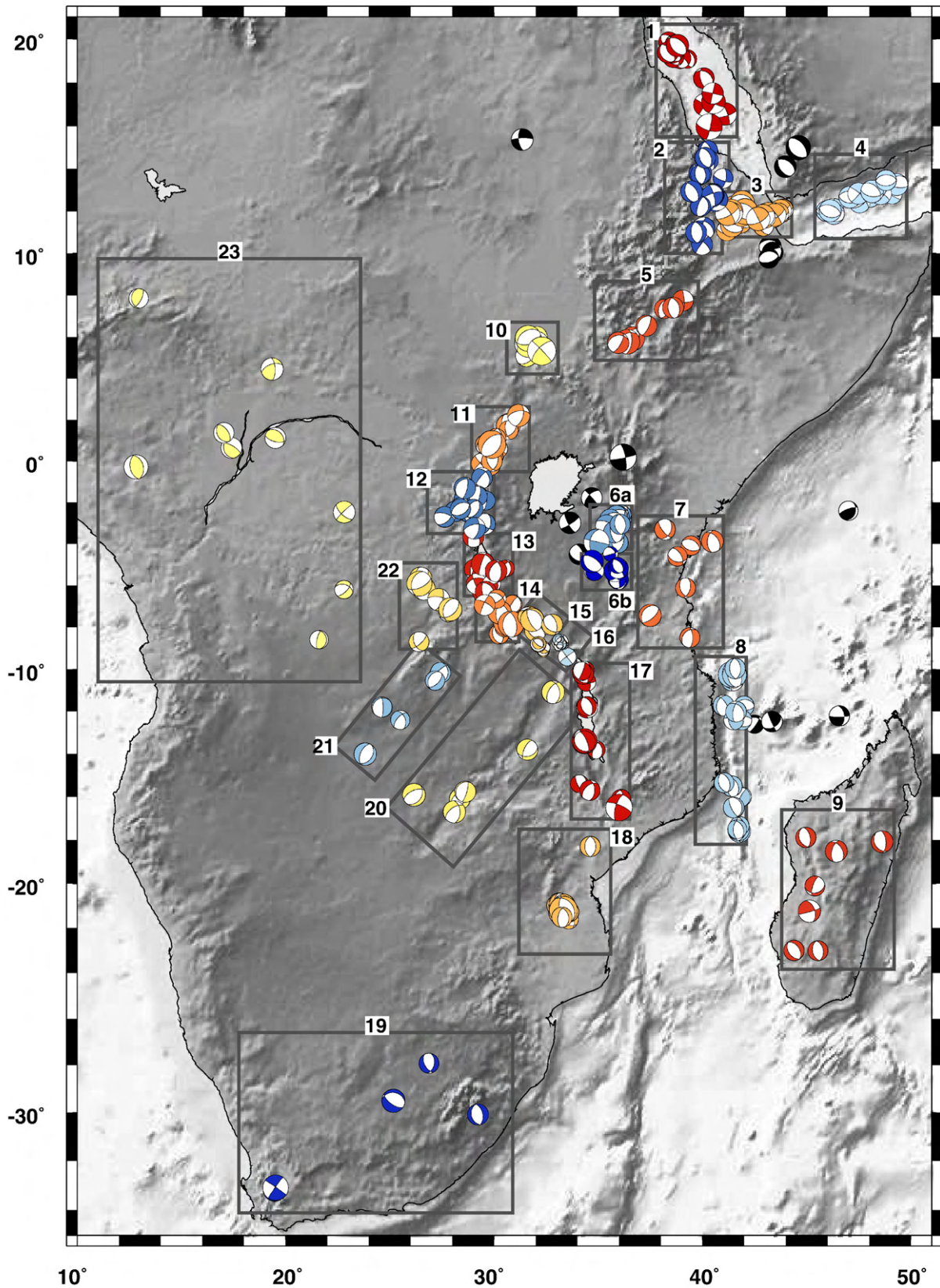


**Fig. 2.** Focal mechanism data assembled into boxes for stress inversion. Boxes: 1 – Red Sea, 2 – Western Afar, 3 – Afar depression, 4 – Gulf of Aden, 5 – Main Ethiopian Rift, 6 – Gregory Rift (6a: Lake Natron, 6b – Manyara–Dodoma), 7 – Indian Coast, 8 – Mozambique Channel, 9 – Madagascar, 10 – South–Sudan, 11 – Albertine Rift, 12 – Rivu Rift, 13 – North–Tanganyika, 13 – South–Tanganyika, 15 – Rukwa Rift, 16 – Mbeya Triple Junction, 17 – Malawi Rift, 18 – Central Mozambique, 19 – South Africa, 20 – Luangwa Graben, 21 – Mweru Graben, 22 – Upemba Graben, 23 – Congo River.

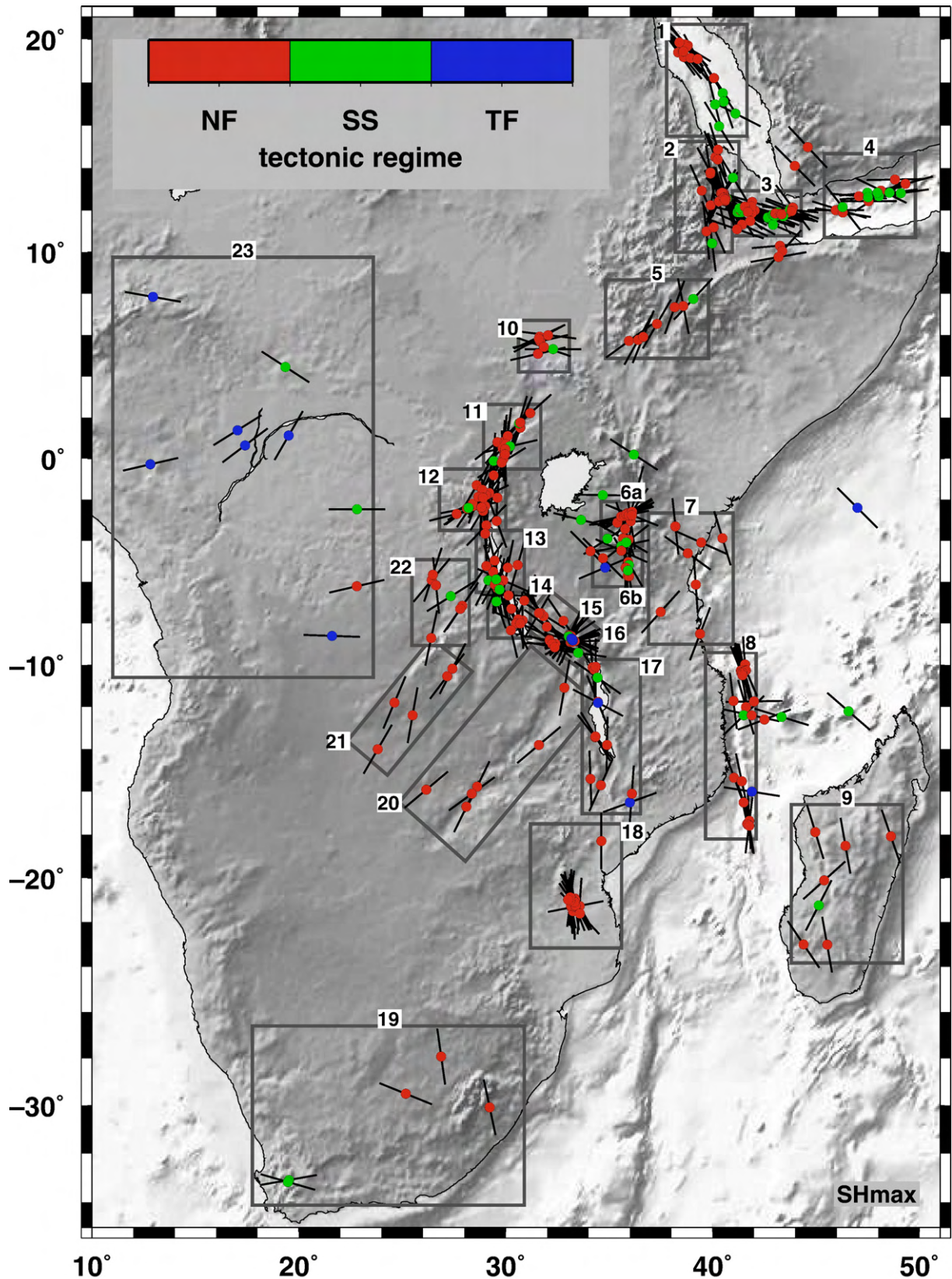


Fig. 3. Focal mechanism data represented as  $S_{Hmax}$  axes. A colour-coded central circle indicates the tectonic regime.

is often the mandatory, two different options exist for heterogeneous focal mechanisms data sets. If applied, the data separation as described above will result in a good quality tensor with a low average misfit angle

but a significant number of data will be excluded from the boxes and the data base will be altered. Another solution which preserves the database would be to use all the data from the boxes instead of only the data that

**Table 2a**  
Stress inversion results for the 24 boxes (parameters of the stress tensor).

Box definition			Reduced stress tensor parameters							Misfit, fluctuation and quality rank					
No	Location	Data	$\sigma_{1pl}$	$\sigma_{1az}$	$\sigma_{2pl}$	$\sigma_{2az}$	$\sigma_{3pl}$	$\sigma_{3az}$	R	$\alpha$ aver	$\alpha$ max	$\sigma$ ( $\alpha$ )	$\tau$	$\sigma( \tau )$	Q
1	Red Sea	16	87	158	03	319	01	049	0.71	8.00	22.9	5.91			A
			62	311	28	143	05	051	0.98	8.63	23.9	6.40	0.97	0.13	A
2	Western Afar	31	86	205	03	348	02	078	0.67	12.59	34.7	9.17			A
			75	177	15	348	02	079	0.58	11.61	48.3	11.41	0.93	0.21	A
3	Afar depression	33	07	292	83	094	02	202	0.66	9.55	33.8	7.37			A
			32	295	58	112	01	204	0.79	9.64	34.6	9.01	0.96	0.13	A
4	Gulf of Aden	15	08	099	79	234	08	008	0.84	9.37	20.5	9.15			A
			10	277	80	082	02	186	0.81	14.91	99.9	24.56	0.87	0.27	B
5	Main Ethiopian Rift	7	76	178	13	029	07	297	0.57	12.54	23.8	7.41			C
			79	239	09	024	06	115	0.79	10.47	31.0	12.70	0.94	0.19	C
6a	Lake Natron	18	77	350	03	244	13	153	0.41	12.27	50.2	11.9			A
			85	000	02	251	05	161	0.37	12.91	28.3	9.92	0.91	0.25	B
6b	Manyara-Dodoma Rift	9	84	091	03	339	05	250	0.54	22.80	108.5	31.2			C
			72	349	18	164	01	255	0.42	28.36	90.4	26.90	0.76	0.26	C
7	Indian Coast	7	75	288	09	158	11	065	0.47	4.45	9.0	2.58			C
			74	303	13	161	10	069	0.45	6.38	13.0	3.99	0.96	0.18	C
8	Mozambique Channel	23	83	328	04	169	03	079	0.48	15.10	117.3	29.33			B
			88	346	02	164	00	254	0.31	17.83	141.8	34.98	0.85	0.18	B
9	Madagascar	7	73	111	10	350	15	258	0.67	4.91	8.8	2.65			C
			73	154	13	012	10	280	0.62	11.89	22.2	6.74	0.93	0.22	C
10	South-Sudan	7	77	072	13	271	04	181	0.82	10.60	25.3	8.46			C
			72	108	16	260	08	352	0.73	12.40	32.0	9.65	0.95	0.13	C
11	Albertine Rift	18	75	296	02	035	15	124	0.32	8.91	27.4	8.2			A
			75	198	15	028	02	297	0.57	14.64	62.4	15.02	0.90	0.23	B
12	Kivu Rift	21	72	257	12	033	13	125	0.27	9.70	38.1	8.05			A
			79	254	08	030	08	121	0.35	9.20	49.3	10.64	0.90	0.27	A
13	North-Tanganyika	16	78	236	04	343	11	074	0.76	20.27	47.9	13.96			B
			71	350	19	186	05	094	0.69	19.72	92.0	24.22	0.85	0.21	B
14	South-Tanganyika	9	76	157	14	323	03	054	0.50	12.37	20.6	6.68			B
			80	149	10	318	02	048	0.38	13.59	29.6	8.96	0.89	0.27	B
15	Rukwa Rift	12	76	161	11	304	08	036	0.30	19.16	62.9	16.12			B
			83	159	06	299	05	029	0.26	16.34	67.3	17.72	0.84	0.29	B
16	Mbeya triple junction	19	15	072	75	250	01	341	0.58	29.01	74.0	22.07			C
			41	085	46	243	11	345	0.58	38.17	110.4	33.71	0.69	0.19	C
17	Malawi Rift	13	83	070	02	333	06	242	0.50	21.87	113.8	30.56			C
			72	301	15	159	10	066	0.34	27.69	140.7	43.13	0.74	0.23	C
18	Central Mozambique	19	82	155	08	348	02	258	0.60	5.74	11.7	3.95			A
			85	084	01	347	05	257	0.53	6.30	16.5	4.18	0.97	0.15	A
19	South Africa	5	65	115	24	301	02	210	0.43	18.63	46.8	15.84			D
			67	283	23	102	01	192	0.48	21.38	34.6	11.12	0.90	0.17	D
20	Luangwa Graben	6	80	215	09	033	01	123	0.53	11.11	21.6	7.62			D
			68	238	20	034	08	127	0.60	4.32	6.2	2.31	0.96	0.19	D
21	Mweru Graben	5	75	229	13	025	05	117	0.53	11.54	18.3	5.89			D
			55	217	34	024	06	118	0.69	6.62	11.4	3.27	0.98	0.11	D
22	Upemba Graben	7	70	249	14	022	14	115	0.61	7.75	13.6	4.3			C
			65	242	19	018	16	114	0.63	7.71	13.8	4.32	0.97	0.15	C
23	Congo River Basin	9	07	096	02	186	83	294	0.54	27.31	133.1	35.83			C
			02	089	26	−002	64	183	0.50	30.72	85.5	26.33	0.78	0.24	C
Total		332													

Box definition: box number, location, number of data in the box; parameters of the reduced stress tensors: plunge (pl) and azimuth (az) of the principal stress axes ( $\sigma_1$ ,  $\sigma_2$  and  $\sigma_3$ ) and stress ratio R; misfit, fluctuation and quality rank:  $\alpha$  aver – average misfit angle,  $\alpha$  max – maximum misfit angle,  $\sigma$  ( $\alpha$ ) – standard deviation of  $\alpha$ ,  $|\tau|$  – normalised shear stress magnitude (for SLICK method only),  $\sigma$  ( $|\tau|$ ) – standard deviation of  $\tau$  (for SLICK method only), Q – quality rank as in Eq. (6).

perfectly misfit to the tensor. This will result in a less well fitting tensor with a higher average misfit angle and thus sometimes a lower quality rank. In the first case, the data heterogeneity can be expressed by the proportion of data used in the inversion relative to the total data set contained in the box while, in the second case, it would be expressed by the average misfit angle and the value of the highest misfit angle.

In the current work, we are using the second option – using all the data present in the boxes, even if it is totally incompatible – to avoid altering the primary data set as the delicate problem of choosing the data to be excluded.

We also perform stress inversions for boxes with five and six FMS, even though this is a very poor database for our analysis. Nevertheless, these inversions can give an important indication for the understanding of the African stress pattern as a whole. On average the boxes contain 14 focal mechanisms with a maximum of 33 events. The 15 remaining data are stand-alone mechanisms that occurred too far from the others, or were in close proximity to each other but in too

small number: 1 from South-Sudan, 2 from Yemen, 3 from South-Afar, 5 from the Gregory Rift and 4 from the Indian Ocean.

## 5. Second and third-order stress field

According to Heidbach et al. (2010-this issue), the tectonic stress field can be classified as a function of the spatial scale of investigation: the 1st order stress field is of continental scale and induced by plate boundaries, 2nd order is of intraplate origin such as continental rifting, isostatic compensation, topography and deglaciation, and the 3rd order corresponds to the detailed stress pattern at the scale of less than 100 km, generated by local density and strength contrasts, structural geometry, topography or active faulting. In this study, in function of the box size and spacing, we typically image the 2nd and the 3rd order stress fields.

In the following paragraphs we discuss the inversion results for all boxes. Resulting quantities as stress orientations, stress ratio, and

**Table 2b**  
Stress inversion results for the 24 boxes (parameters for stress map).

Box definition			Quality		Tectonic stress regime				Horizontal stress axes SH					
No	Region	Data	$\alpha$ aver.	Q	Reg.	R'	Aver.	Diff.	S <sub>Hmax</sub>	Aver.	S <sub>Hmin</sub>	Aver.	Diff.	
1	Red Sea	16	8.00	A	NF	0.71	0.84	0.27	139	139.9	49	49.9	1.7	
			8.63	A	NF	0.98				141		51		
2	Western Afar	31	11.26	A	NF	0.67	0.63	0.09	170	169.7	80	79.7	0.6	
			11.61	A	NF	0.58				169		79		
3	Afar depression	33	9.68	A	SS	1.34	1.28	0.13	112	113.1	22	23.1	2.1	
			9.64	A	SS	1.21				114		24		
4	Gulf of Aden	15	10.15	A	SS	1.16	1.18	0.03	98	97.2	8	7.2	1.7	
			14.91	B	SS	1.19				96		6		
5	Main Ethiopian Rift	7	8.83	C	NF	0.57	0.68	0.22	26	25.7	116	115.7	0.7	
			10.47	C	NF	0.79				25		115		
6a	Lake Natron	18	9.29	A	NF	0.43	0.40	0.06	62	66.5	173	167.0	12.0	
			12.91	B	NF	0.37				71		161		
6b	Manyara-Dodoma Rift	9	24.40	C	NF	0.54	0.48	0.12	162	163.6	72	73.6	3.3	
			28.36	C	NF	0.42				165		75		
7	Indian Coast	7	4.42	C	NF	0.47	0.46	0.02	153	154.8	63	64.8	3.5	
			6.38	C	NF	0.45				157		67		
8	Mozambique Channel	23	15.10	B	NF	0.48	0.40	0.17	169	166.5	63	68.5	10.9	
			17.83	B	NF	0.31				164		74		
9	Madagascar	7	5.17	C	NF	0.67	0.65	0.05	167	177.7	77	87.7	21.3	
			11.89	C	NF	0.62				188		98		
10	South-Sudan	7	10.25	C	NF	0.82	0.77	0.09	91	87.1	181	177.0	7.7	
			12.40	C	NF	0.73				83		173		
11	Albertine Rift	18	9.37	A	NF	0.32	0.44	0.25	35	30.8	125	120.8	8.3	
			14.64	B	NF	0.57				27		117		
12	Kivu Rift	21	9.62	A	NF	0.27	0.31	0.08	42	37.7	132	127.7	8.7	
			9.20	A	NF	0.35				33		123		
13	North-Tanganyika	16	18.56	B	NF	0.76	0.73	0.07	164	174.0	74	84.0	11.3	
			19.72	B	NF	0.69				184		94		
14	South-Tanganyika	9	13.49	B	NF	0.50	0.44	0.12	145	141.7	55	51.7	6.5	
			13.59	B	NF	0.38				138		48		
15	Rukwa Rift	12	19.16	B	NF	0.30	0.28	0.04	130	125.4	40	35.4	6.3	
			16.34	B	NF	0.26				121		31		
16	Mbeya triple junction	19	27.01	C	SS	1.42			72	75.0	162	165.0	5.9	
			38.17	C	U					78		168		
17	Malawi Rift	13	20.91	C	NF	0.50	0.42	0.16	152	151.5	62	61.5	0.9	
			27.69	C	NF	0.34				151		61		
18	Central Mozambique	19	5.70	A	NF	0.60	0.56	0.07	169	167.7	79	77.7	2.6	
			6.30	A	NF	0.53				166		76		
19	South Africa	5	18.63	D	NF	0.43	0.45	0.05	119	110.6	29	20.6	16.8	
			21.38	D	NF	0.48				102		12		
20	Luangwa Graben	6	12.91	D	NF	0.53	0.57	0.07	33	36.1	123	126.1	2.2	
			4.32	D	NF	0.60				39		129		
21	Mweru Graben	5	11.54	D	NF	0.53	0.61	0.16	28	28.8	118	118.8	1.6	
			6.62	D	NF	0.69				30		120		
22	Upemba Graben	7	7.75	C	NF	0.61	0.62	0.02	27	27.0	117	117.0	0.1	
			7.71	C	NF	0.63				27		117		
23	Congo River Basin	9	28.31	C	TF	2.54	2.52	0.04	96	92.7	6	2.7	6.5	
			30.72	C	TF	2.50				89		— 1		
Total		332						Average diff.					6.6	
									Max. diff.					21.3
										Sandart Dev.				

Box definition as in Table 2a; Quality:  $\alpha$  aver. — average misfit angle, Q — quality rank as in Eq. (6); Tectonic stress regime: Reg. — stress regime according to the WSM standard, R' — stress regime index according to Eq. (5), with average (aver.) and difference (diff.) for/between the two methods; Horizontal stress axes expressed clockwise from the North: S<sub>Hmax</sub> and S<sub>Hmin</sub> with average (aver.) and difference (diff.) for/between the two methods.

misfit angle are given for each box, for both methods (upper value from TENSOR, lower value from SLICK: Table 2a and 2b). The corresponding equal-area stereoplots are shown on Fig. 4 for TENSOR and Fig. 5 for SLICK. The results are represented on map view in function of the stress regimes and horizontal stress axes orientation (Fig. 6).

### 5.1. Red Sea–Afar–Gulf of Aden (boxes 1–4)

The Afar Rift triple junction is a key point in the Arabia, Nubian and Somalia plate kinematics (Garfunkel and Beyth, 2006). The Red Sea box (1) highlights the divergence between the Nubia and Arabia plate, dominantly by normal faulting (11 events) and partly by strike-slip faulting (5 events). The resulting stress tensor suggests that extension is homogeneous in a NE–SW orientation (N049/051°E), and the combination of normal and strike-slip faulting is expressed by the relatively high stress ratio R' (0.71/0.98). A similar situation occurs in Western Afar

(box 2), but the average orientation of extension rotated clockwise to more E–W (N080/079°E). The Afar Depression box (3) contains a larger proportion of strike-slip focal mechanisms (14 SS out of 33 events and 5 intermediate (NS)). The inverted stress field has a nearly N–S S<sub>Hmin</sub> orientation (N022/024°E), but with a SS regime (R' = 1.34/1.21). The stress field in the Gulf of Aden (box 4) lies in continuity of the Afar Depression stress field, with a slightly anticlockwise rotated S<sub>Hmin</sub> (N008/006°E) and still a SS regime (5 SS events out of 15) but a bit more extensional (R' = 1.16/1.19).

### 5.2. Eastern Branch (boxes 5–6)

Only 7 focal mechanisms exist for the Ethiopian Rift (box 5) and all of them show ESE–WNW S<sub>Hmin</sub> orientation, consistent with field observations (Ebinger and Casey, 2001; Casey et al., 2006) and also with the relative opening orientation between the Nubian and

Somalian plates (Calais et al., 2006). The formal stress inversion results in a N116/115°E  $S_{\text{hmin}}$  and a NF regime with a slight strike-slip component ( $R' = 0.57/0.79$ ).

For the Gregory Rift in Central Kenya only one focal mechanism is available (the January 1928  $M_w$  6.7 event: Doser and Yarwood, 1991). From the geological fault-slip data and the displacement of quaternary

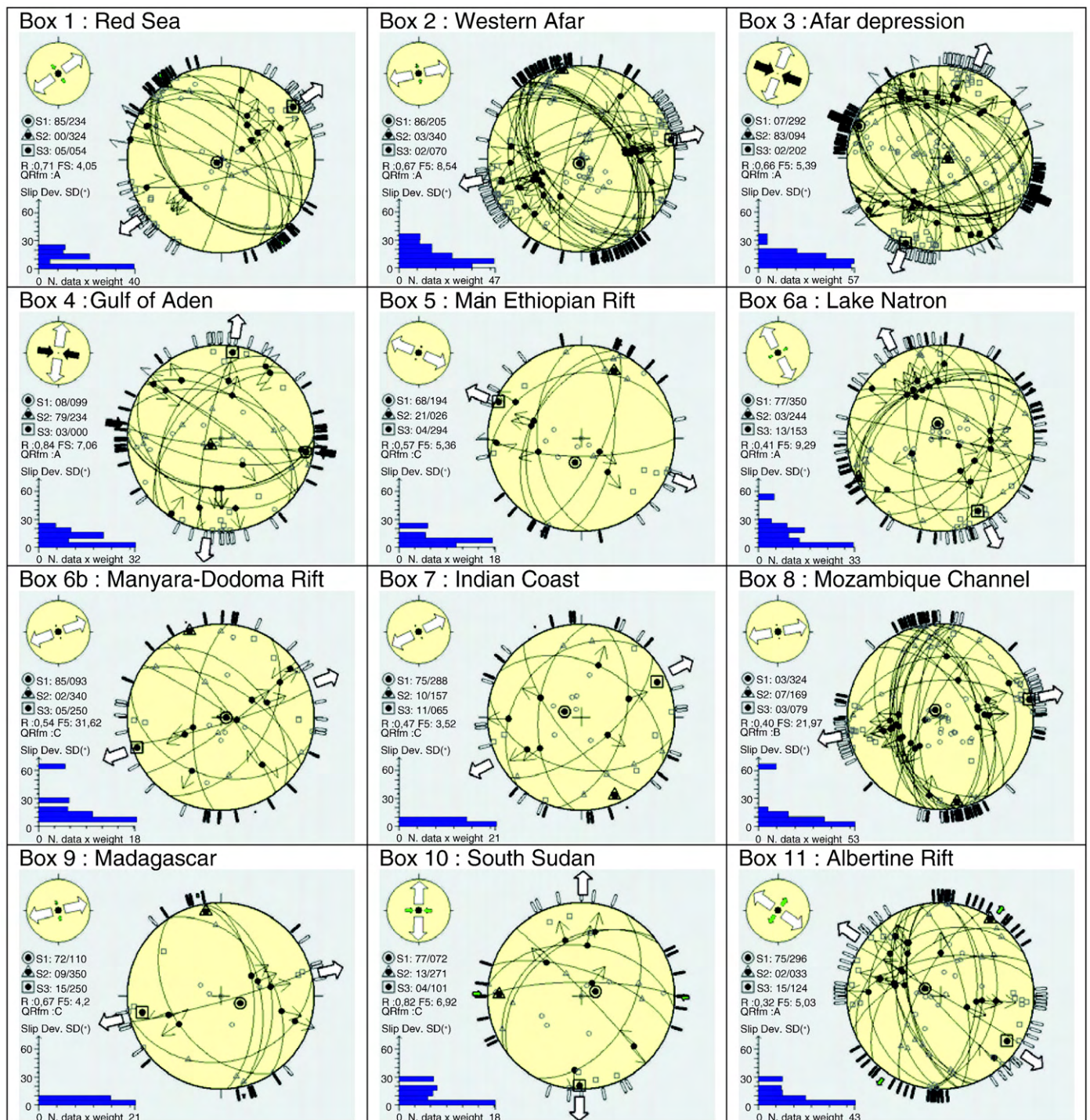


**Fig. 4.** Lower-hemisphere equal-area stereoplots of the selected focal planes (shown as cyclographic trace) and associated slip lines (black dot with outward arrow for normal faulting, inward arrow for reverse faulting and double semi-arrows for strike-slip faulting). Stress inversion results are represented by the orientation of the 3 principal stress axes (a black dot surrounded by a circle for  $\sigma_1$ , a triangle for  $\sigma_2$  and a square for  $\sigma_3$ ). The related  $S_{\text{Hmax}}$  and  $S_{\text{hmin}}$  orientations are represented by large arrows outside the stereogram. Their type, length and colour symbolise the horizontal deviatoric stress magnitude relative to the isotropic stress ( $\sigma_i$ ) and are in function of the stress regime and the stress ratio  $R = \sigma_2 - \sigma_3 / \sigma_1 - \sigma_3$ . White arrows when  $\sigma_3$  is subhorizontal (always  $S_{\text{hmin}}$ ), green arrows when  $\sigma_2$  is subhorizontal (either  $S_{\text{hmin}}$  or  $S_{\text{Hmax}}$ ), black arrows when  $\sigma_1$  is subhorizontal (always  $S_{\text{Hmax}}$ ). Outward arrow indicates extensional deviatoric stress ( $<\sigma_i$ ) and inward arrows, compressional deviatoric stress ( $>\sigma_i$ ). The vertical stress ( $\sigma_v$ ) is symbolised in the small circle with stress arrows on the upper left corner of the figures by a solid circle for extensional regimes ( $\sigma_1 \approx \sigma_v$ ), a dot for strike-slip regimes ( $\sigma_2 \approx \sigma_v$ ) or an open circle for compressional regimes ( $\sigma_3 \approx \sigma_v$ ). The histogram on the lower left corner of the figures represents the distribution of the misfit angle  $\alpha$  (Slip.Dev. SD), weighted arithmetically according to the magnitude. The contribution of data with misfit angles  $>65^\circ$  are all summed up and represented together along the vertical axis between  $\alpha$  at the 60–65° interval (sites 6b, 8, 16, 17, 23). The bars outside the stereogram represent the  $S_{\text{Hmax}}$  (black) and  $S_{\text{hmin}}$  (white) directions for individual focal mechanisms and the small grey symbols inside, the orientations of the related kinematic axes (circle:  $p$  axis, triangle:  $b$  axis, square:  $t$  axis).

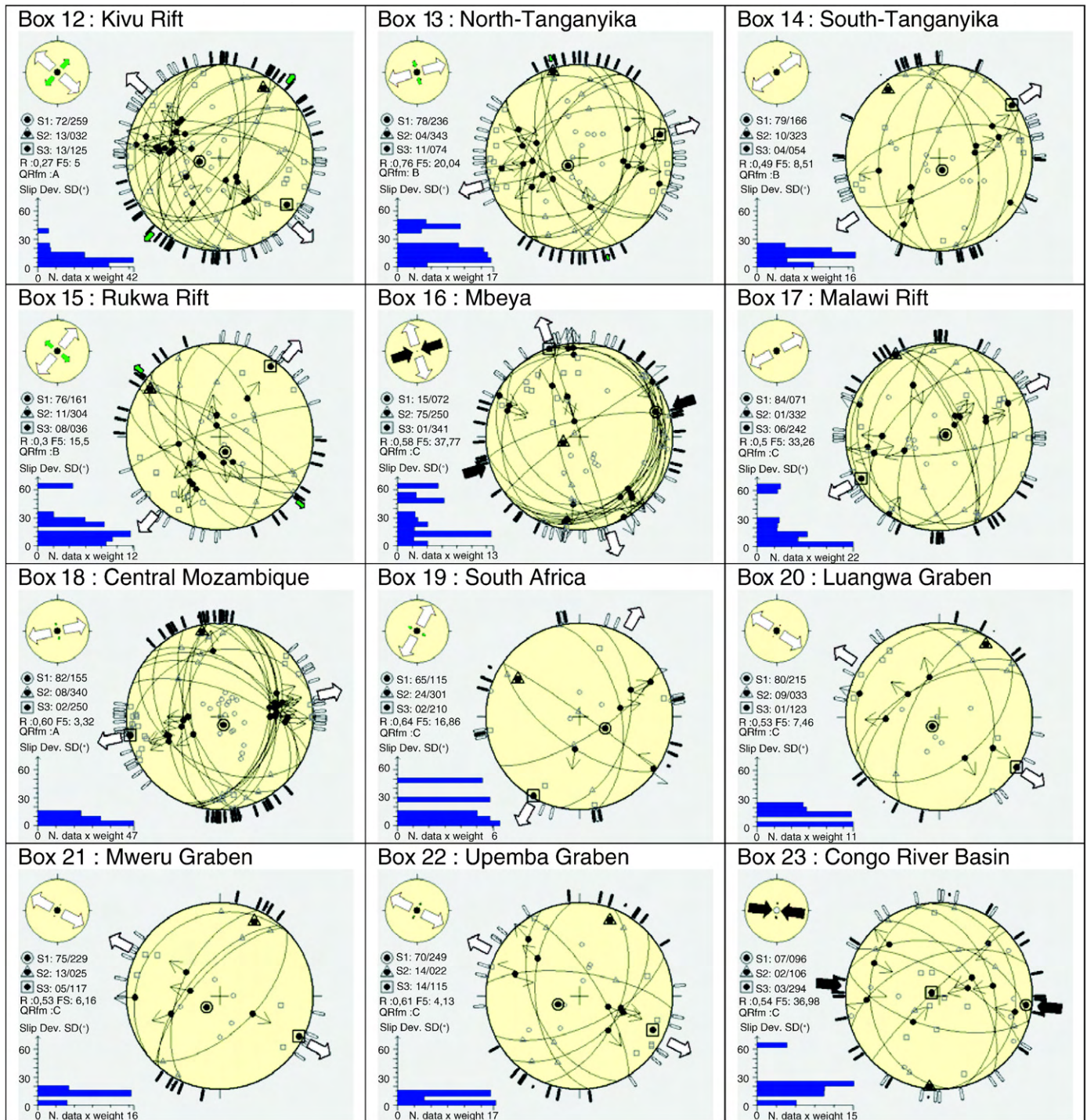
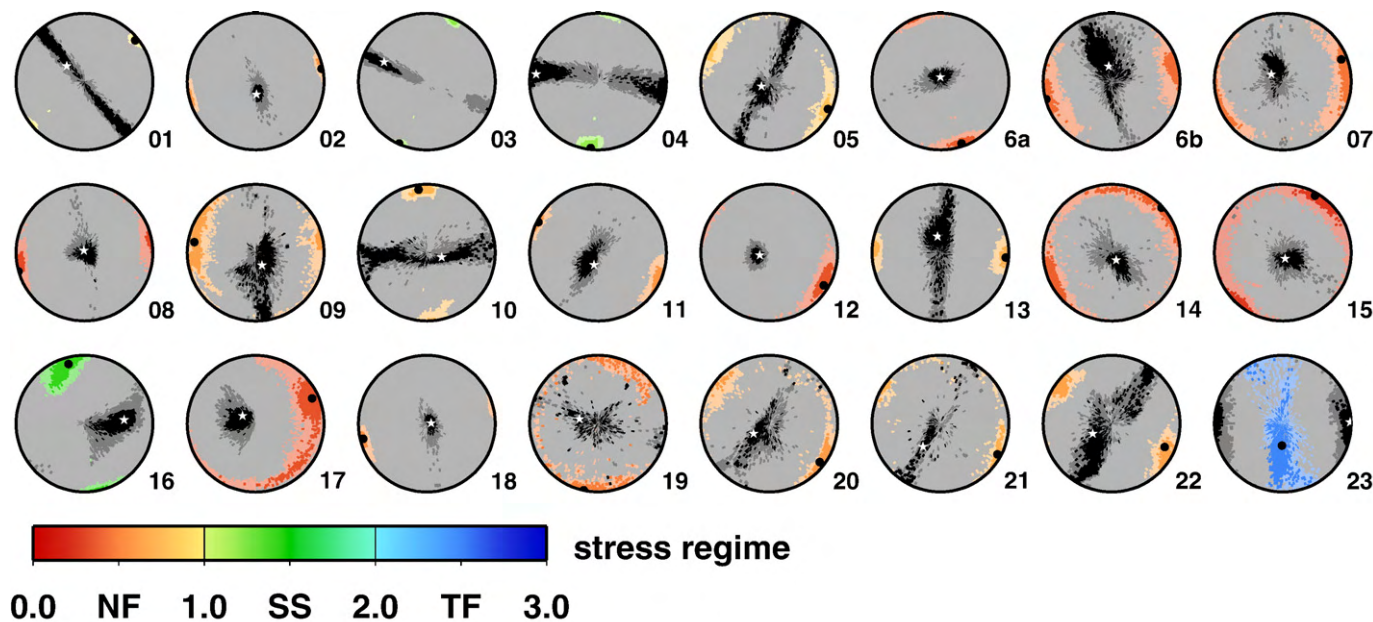


Fig 4 (continued).

volcanic vents, [Strecker et al. \(1990\)](#) deduced that the Late Quaternary orientation of extension should be trending NW–SE. In the Lake Magadi area in South Kenya, [Ibs-von Seht et al. \(2001\)](#) obtained a composite focal mechanism with E–W  $S_{hmin}$  from a seismic swarm studied by a temporary seismic network. More to the South, the 2007 Natron volcano-seismic crisis is associated to a slow slip on a relatively low angle normal fault with NNW–SSW  $S_{hmin}$  ([Calais et al., 2008](#)). The southern part of the Gregory Rift extends into Central Tanzania, forming the Manyara–Dodoma Rift segment, for which an ENE–WSW extension was found ([Macheyeki et al., 2008](#)). This evidences the rapid lateral variations of stress field within the same rift structure,

possibly related to local density contrasts at the margin of the Tanzanian Craton, structural complexity, and inheritance from older structures.

Except for the 1928 event, all focal mechanisms available for the Gregory Rift (box 6) are located in North and Central Tanzania. They present a wide variety of  $S_{Hmax}$  orientations, especially in between 3° and 5° latitude South, in the area of the Ngorongoro crater and Lakes Eyasi and Natron. A first trial to adjust a single stress tensor on the total number of 32 focal mechanisms proved unsuccessful. In order to define regions with a more homogeneous stress field, we split box 6 into two smaller boxes (6a: Lake Natron and 6b: Manyara–Dodoma



**Fig. 5.** Equal-area stereoplots of confidence regions for the orientation of the principle axes from the SLICK method for each analysed box. Dark and bright areas show the 50% confidence regions for  $\sigma_1$  and  $\sigma_3$ , respectively. The colour-coding of  $\sigma_3$  indicates the stress regime index  $R'$  (Eq. 5). The greater shaded areas show the 95% confidence regions. The orientation of the best-fit  $\sigma_1$  and  $\sigma_3$  is shown by a white star and a black dot, respectively.

Rift) containing 18 and 9 focal mechanisms, respectively. This left 5 data from the Gregory Rift area as stand alone. The Natron box (6a) is dominated by 10 focal mechanisms related to the 2007 Natron volcano-seismic crisis. The resulting stress tensor is of NF type ( $R' = 0.43/0.37$ ) with a NNE oriented  $S_{\text{hmin}}$  (N173/161°E) and a very good quality (A/B). For the Manyara–Dodoma Rift, the stress inversion of the 9 events in box 6b gives results which are close to the one obtained from a selection of 12 focal mechanisms in [Macheyeki et al. \(2008\)](#):  $R' = 0.54/0.42$ ,  $S_{\text{hmin}} = \text{N072}/075^\circ\text{E}$  in the present study and  $R' = 0.50$  and  $S_{\text{hmin}} = \text{N082}^\circ\text{E}$  in the previous study. The relatively large average misfit angle (24.4/28.4°) reflects the high data heterogeneity (also seen in [Fig. 4](#) by the high dispersion of the SH axes and in [Fig. 5](#) by a widely scattered confidence region for  $\sigma_1$ ). In both cases, the stress regime is of pure NF type and the orientation of extension (ENE–WSW) is more as would be expected from the neighbouring Indian Coast (box 7) but in sharp contrast with the one of the Natron box (6a).

### 5.3. Indian Coast to Madagascar (boxes 7–9)

South of the Manyara–Dodoma Rift in Central Tanzania, active extensional deformation associated to the Eastern Branch of the EARS seems to jump laterally to the coastal region and the Indian Ocean. The coastal regions of Kenya and Tanzania (Indian Coast, box 7) display homogeneous extension in an ENE–WSW (N063/067°E) orientation and a pure NF regime ( $R' = 0.47/0.45$ ). Between Mozambique and Madagascar, the Mozambique Channel is known for its seismicity associated mainly to the Davie Ridge ([Grimison and Chen, 1988](#)). The Mozambique Channel (box 8) shows a similar ENE–WSW (N063/067°E) extension with NF, as does also Madagascar further South (box 9, N077/098°E extension). The stress regime is more radial for the Mozambique Channel ( $R' = 0.48/0.31$ ) and more strike-slip for Madagascar ( $R' = 0.67/0.62$ ).

Following [Nicholas et al. \(2007\)](#), Miocene rifting occurred along the southern coastal Tanzania, but post-Miocene compressive inversion structures with reverse and thrusts faults are seen in the field and on the seismic profiles. They show that southern coastal Tanzania has been submitted to compression and strike-slip deformation since the last 6 Ma. However, the present deformation regime as shown by the

focal mechanisms is clearly extensional. This reflects unstable interactions between the Rovuma and Somalia plates since the Pliocene, with episodic compression and extension periods.

### 5.4. South Sudan (box 10)

In 1990–1991 an earthquake sequence with two events reaching  $M_W$  7.1 occurred in South Sudan north of the Albert Nile, in an area previously devoid of marked seismicity and without well expressed rift-related morphostructures. It was interpreted as marking the northern extension of the Western Branch of the EARS north of the Aswa lineament ([Gaulon et al., 1992](#); [Girdler and McConnell, 1994](#)). A total of 7 CMT solutions are available. The first event, and also the largest, is a strike-slip faulting mechanism that is interpreted by [Gaulon et al. \(1992\)](#) as reactivating the NW trending Aswa lineament in a left-lateral way. From the other events, four of them show typical normal faulting and two oblique faulting, intermediate between normal and strike-slip. Despite this variety, they all display N–S  $S_{\text{hmin}}$ . The stress inversion results indicate N–S extension ( $S_{\text{hmin}} = \text{N001}/173^\circ\text{E}$ ) and a NF stress regime with a strong strike-slip component ( $R' = 0.82/0.73$ ), consistently with the single-event data.

### 5.5. Northern part of the Western Branch (boxes 11–12)

The northern part of the Western Branch of the EARS is well marked by the Albertine Rift (which includes the Albertine Graben, Semliki Basin and Rwenzori Mountains) and the Kivu Rift ([Ebinger, 1989](#); [Upcott et al., 1996](#); [Karner et al., 2000](#); [Laerdal and Talbot, 2002](#); [Koehn et al., 2008](#)).

Detailed investigations of the Albertine Graben for petroleum exploration ([Abeinomugisha and Mugisha, 2004](#); [Abeinomugisha, 2007](#)) reveal that rifting originated in late Oligocene or Early Miocene, followed by a short episode of compression during mid-Miocene, which generated flower structures and anticlines. A second phase of rifting occurred in the Pliocene, followed again by a short episode of compression during the Pleistocene. The present-day fault kinematics as evidenced by the focal mechanisms (box 11, Albertine Rift) is back to NF under NW–SE extension (N125/117°E  $S_{\text{hmin}}$ ,  $R' = 0.32/0.57$ ). Most of

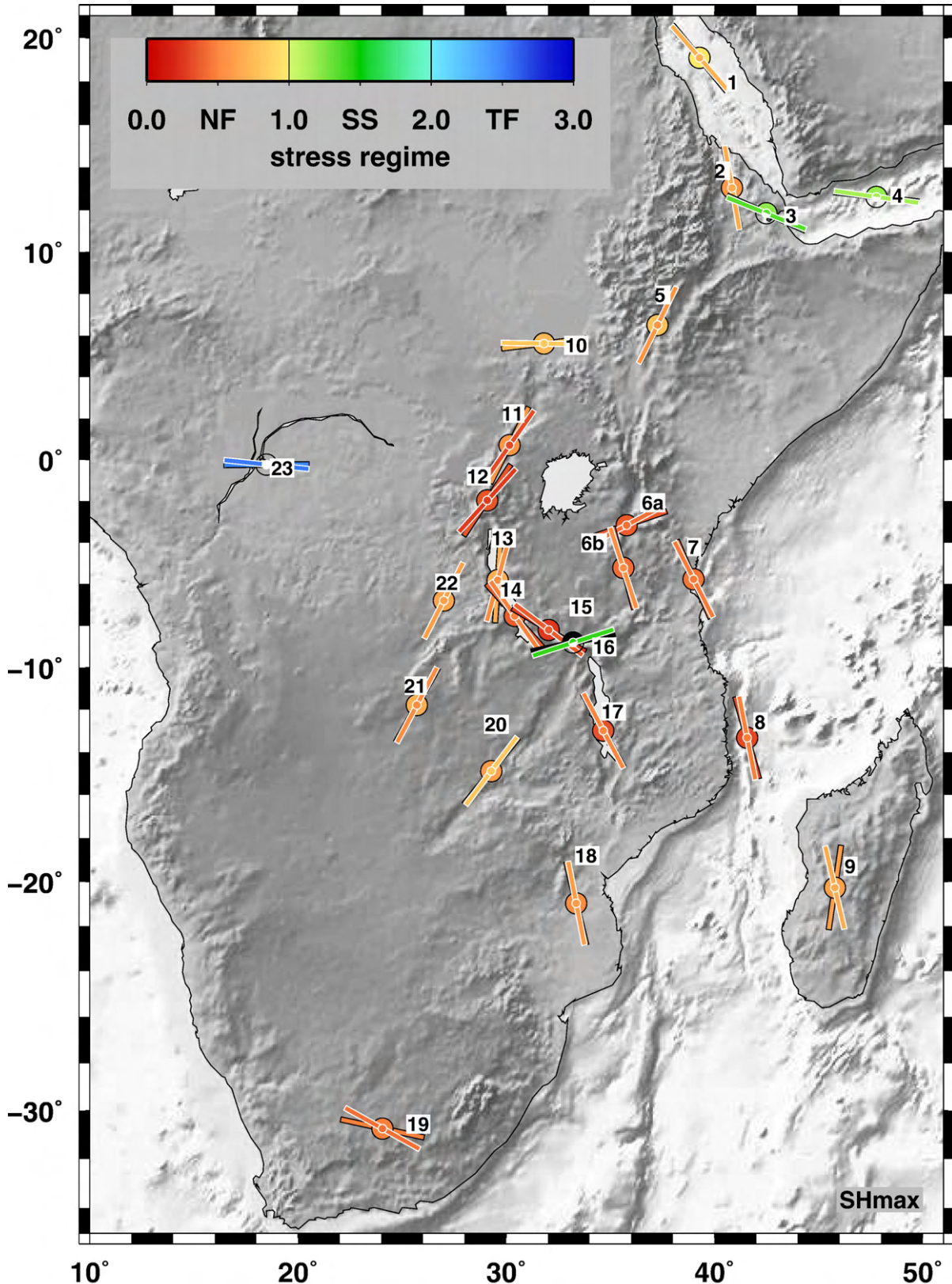


**Fig. 6.** Map representation of the stress inversion results for each box. The horizontal stress axes ( $S_{Hmax}$ ) are represented by thick bars with a narrow central circle and white borders (TENSOR) or a large central circle and black borders (SLICK). The filling colour is coded in function of the stress regime index  $R'$ .

the recorded focal mechanisms come from the couple Semliki Basin–Rwenzori Mountains at the south of this block and are of normal faulting type. Only one of them is strike-slip.

The area of Lake Kivu (box 12) (Ebinger, 1989) is another node of high seismicity in the Western Branch, hosting also the Virunga volcanic province. It has been studied as early as in the 1950's (De Bremaeker,

1956). All the 21 focal mechanisms display a normal faulting mechanism, some of which are oblique. Although the general trend of the rift is N–S, as opposed to the NE–SW trend of the Albertine–Rwenzori segment, extension remained NW–SE (N132/123°E  $S_{\text{hmin}}$ ). The stress regime is also NF, a bit more radial ( $R' = 0.27/0.35$ ).

#### 5.6. Central part of the Western Branch (boxes 13–15)

Lake Tanganyika occupies the central part of the Western Branch. Extension in some parts of the basin initiated as early as in the Karoo times (Sander and Rosendahl, 1989; Delvaux, 1991). The stress inversion for North Tanganyika (box 13) gives an ESE–WNW  $S_{\text{hmin}}$  (N74/094°E) under NF regime, but with a slight strike-slip component ( $R' = 0.76/0.69$ ) as opposed to the radial component of the Kivu Rift box ( $R' = 0.27/0.35$ ). The southern half of Lake Tanganyika (box 14) belongs to the TRM (Tanganyika–Rukwa–Malawi) rift segment, along which the kinematic model of Chorowicz (2005) infer dextral strike-slip movements under NW–SE extension. Instead, the focal mechanism inversion gives a pure NF regime even slightly radial with SLICK ( $R' = 0.49/0.38$ ) under an NE–SW extension (N055/048°E  $S_{\text{hmin}}$ ), almost orthogonal to the NW–SW rift trend.

The Rukwa Rift which forms the central part of the TRM segment has also been studied for hydrocarbon exploration (Kilembe and Rosendahl, 1992; Morley et al., 1992) and for its neotectonic activity (Delvaux et al., 1998). It contains thick series of Karoo, Cretaceous, Early Cainozoic and Miocene–Recent sediments. Inversion tectonic structures have been evidenced in the industrial seismic profiles (Morley et al., 1999) and a high-resolution seismic survey shows that some faults are still active in its centre (Morley et al., 2000). In addition, the Ufipa Plateau between the Rukwa and the South Tanganyika depression is affected by the 160 km-long Kanda active normal fault that might have generated the 1910 Ms 7.4 earthquake, which is still the strongest ever recorded in the East African Rift (Vittori et al., 1997). For this box (15), both the large- and small-magnitude earthquakes show consistently NE–SW extension, orthogonal to the rift trend. The resulting  $S_{\text{hmin}}$  orientation (N040/031°E) and NF regime with a radial component ( $R' = 0.30/0.26$ ) are consistent with the observed geological fault-slip indicator along the Kanda active fault (unpublished data; Delvaux et al., 2007). The same comparison with the kinematic model of Chorowicz (2005) as above applies here also.

#### 5.7. Mbeya triple junction (box 16)

The Mbeya box lies at the triple junction between the Somalia, Victoria and Rovuma plates (Ebinger et al., 1989; Delvaux and Hanon, 1993). It contains the Rungwe volcanic province and links the NW-trending South Rukwa and North Malawi rift basins with the NE-trending Usangu basin. The latter belongs to the ill-defined tectonic boundary between the Victoria and Rovuma plates (Calais et al., 2006). This area has also a complex tectonic evolution since the Karoo times, dominated by normal faulting, but also affected by compression tectonic pulses (Delvaux et al., 1992; Ring et al., 1992; Delvaux et al., 1998). Since the Middle Pleistocene, it lies in a strike-slip setting as shown by a geological fault-slip data in dated sediments and volcanic rocks. All but one of the focal mechanisms from this box has been determined from micro-earthquakes recorded by a temporary seismic network (Camelbeek and Iranga, 1996; Ferdinand and Arvidsson, 2002a,b). The focal planes combine high-angle and low-angle focal planes with a large dispersion of  $S_{\text{Hmax}}$  orientations (Fig. 4, continued). They resulted in a stress tensor with a rather large average misfit angle  $\alpha$  (27.01°/38.17°), witnessing the internal heterogeneity. The  $S_{\text{hmin}}$  orientation is NNW–SSE (N162/168°E), almost orthogonal to the Usangu Depression but parallel to the trend of the TRM. The TENSOR method gives a relatively stable SS stress tensor ( $R' = 1.42$ ) with a

subhorizontal  $\sigma_1$  axis and a subvertical  $\sigma_2$  axis while the SLICK method (Fig. 5) gives a 41° plunging  $\sigma_1$  and the confidence region does not show a clear regime (either SS or NF).

#### 5.8. Southern part of the Western Branch (boxes 17–18)

The Western Branch of the EARS continues south of the Mbeya triple junction by the Malawi Rift (box 17) and by more weakly expressed asymmetric structures along the coastal region of Central Mozambique (box 18). The Malawi Rift was the location of a strong normal faulting earthquake in March 1989 (Jackson and Blenkinshop, 1993), later associated to a 100 km-long active fault (Jackson and Blenkinshop, 1997). More recently, in February 2006 a  $M_w$  7.0 earthquake occurred in the coastal region of Central Mozambique and generated a surface fault rupture observed over 15 km, with a possible overall extension of 30 km, with a vertical separation from 0.4 to 2.05 m and a component of left-lateral displacement of max 0.7 m (Fenton and Bommer, 2006). The fault plane appears exceptionally steep, dipping 76°± (Yang and Chen, 2008). It was followed by numerous aftershocks, from which 16 CMT focal mechanisms could be determined. This crisis occurred in a region of subtle topography with apparent lack of prior faulting morphology. Both boxes yielded well-constrained stress tensors with ENE–WSW  $S_{\text{hmin}}$  (062/061°E and N079/076°E) and under pure NF regime ( $R' = 0.50/0.34$  and 0.60/0.53).

#### 5.9. South-western High Plateau region in Katanga–Zambia (boxes 20–22)

The south-western High Plateau region of the Nubian plate, west of the TRM rift segment, is affected by a series of NE-trending grabens in the Katanga province of the RDC and in Zambia. They might correspond to incipient continental breakup in the middle of the Nubian plate (Sebagenzi and Kaputo, 2002), but the apparent velocity difference between West Africa and South Africa (where GPS data are available up to now) did not justify for a new plate separation in the kinematic model of Calais et al. (2006).

The Luangwa (box 20), Mweru (box 21) and Upemba (box 22) graben regions show a similar  $S_{\text{hmin}}$  orientation, in a NW–SE orientation (between N117°E and N129°E), orthogonal to the incipient rift structures. They present a NF regime with a very slight strike-slip component (respectively  $R' = 0.53/0.60$ , 0.53/0.69 and 0.61/0.63). From these three boxes, only the Upemba Graben (box 22) has a SS and a NS focal mechanism while all the others are NF. A large number of hot thermal springs are known in the region, especially in the vicinity of the Upemba Graben (Robert, 1956).

#### 5.10. Intraplate settings (boxes 19, 23)

The two remaining boxes are not associated with rifting: South Africa (box 19) and Congo River Basin (box 23). They are in intraplate settings and likely represent the first-order stress field, away from the influence of the Cainozoic rift and associated high relief. Studying the South African stress and strain pattern using stress data from borehole and fault slip data, Bird et al. (2006) observed a NW–SE oriented  $S_{\text{Hmax}}$  which they associate with a resistance to the Nubia–Somalia extension. Concerning tectonic earthquake sources, South Africa (box 19) is poorly illustrated by only five focal mechanisms. The inverted stress regime is of NF with a slight radial component ( $R' = 0.43/0.48$ ) and an N–S  $S_{\text{hmin}}$  (N029/012°E).

The wide Congo River Basin (box 23), which develops over an old cratonic crust between the Western Branch of the EARS and the Atlantic coast, has a moderate seismicity, probably associated to its deep structure concealed under the Cretaceous to Cainozoic sediments (Daly et al., 1992). The presence of low magnitude reverse events in the Congo River Basin was highlighted by Ayele (2002). This

is intriguing as they are coincident with a large negative free-air gravity anomaly, an anomalous topographic depression and a large positive upper-mantle shear-wave velocity anomaly (Pasyanos and Nyblade, 2007; Downey and Gurnis, 2009). From the nine focal mechanisms compiled, seven are TF, one SS and one NF. According to the adopted procedure, we keep all of them and obtained a pure TF type ( $R' = 2.54/2.50$ ) with an almost N–S  $S_{\text{hmin}}$  orientation (N186/179°E) with a C quality. The large average misfit angles (28.31°/30.72°) reflect largely the inclusion of the NF mechanism within dominantly TF ones (see also Figs. 4 and 5).

## 6. Discussions

### 6.1. Sensitivity of the interpretation and results to the box boundaries

During the delicate step of data selection through the definition of the box boundaries, both methods showed the same order of variation. The choice of the box boundaries was made in order to restrict the coverage area of the subset to a minimum, with the greatest density of similar focal mechanisms. The principal difficulties were the determination of the boundaries of boxes 6a and 6b, as the stress field changes rapidly in the Tanzanian sector of the Gregory Rift and there is a spatial mixing of focal mechanisms of different types and orientations. We first started to group them in a single box, and owing to the too large misfits, we choose to divide it in two (6a and 6b). For these two sub-boxes, the results obtained were significantly dependent on the choice of the box boundaries. Box 8 (Mozambique Channel) could be extended further seaward, but we wanted it to represent the tectonic stress of the Davies Ridge and thus we excluded the 3 intraplate events east of it. Integrating these 3 events within box 8 did not change significantly the stress results, but degraded the overall quality by increasing the misfits. For all the other boxes, the box definition was obvious and no difficulties arose.

### 6.2. Similarities and differences between the two methods

Both the TENSOR and SLICK stress inversion methods provide stable and reliable results for most of the 24 boxes. The results also compare well between the two methods, for the stress axis orientation as well as for the stress regimes (Table 2b). This highlights the robustness of the conclusions.

In terms of stress orientations, the average difference in  $S_{\text{Hmax}}$  orientations between the two methods is 6.0°, with a standard deviation of 5.5° and a maximal value of 21.3°. Inversion results may vary and show instabilities only for boxes with a small number of focal mechanisms (21.3° for box 9 with 7 data and 16.8° for box 19 with 5 data). Similarly, the tectonic stress regimes obtained are also comparable between the two methods. The average difference in the tectonic stress index  $R'$  is 0.10, with a standard deviation of 0.07 and a maximal value of 0.27. Differences larger than 0.2 are found for boxes 1 and 11 although, for both of them, the number of data is relatively large (respectively 16 and 18). For some regions we find the  $\sigma_3$  axis to be nearer to the ideal vertical position using the TENSOR program than using the SLICK method. This might be due to the different minimisation functions and weighting. For the average misfit angle  $\alpha$ , values from both methods are comparable, with a tendency to be slightly lower for the TENSOR method.

The confidence regions of the principal stress axes, which are calculated for the SLICK method by a statistical bootstrap analysis, are shown in Fig. 5. Narrow and focused confidence regions for both  $\sigma_1$  and  $\sigma_3$  axis are typical for boxes with high quality (A) stress tensors (boxes 2, 6a, 12, 18). However, some A and B quality solutions show focused confidence only for  $\sigma_3$ , while  $\sigma_1$  is restricted on orientations orthogonal to  $\sigma_3$  (boxes 1, 3, 4, 13). This means that both, NF and SS regimes could explain the data, while the horizontal stress axes remain constant. This agrees well with the presence of mixed NF and

SS individual focal mechanisms in these boxes (Table 1) with sub-parallel kinematic  $t$  axes (tension) and both  $b$  (intermediate) and  $p$  (compression) axes distributed along a girdle, leading to a narrow dispersion of individual  $S_{\text{Hmax}}$  and  $S_{\text{hmin}}$  axes (Fig. 4). For these boxes, the tectonic stress index  $R'$  typically ranges in the intermediate NF to SS field, between 0.69 and 1.34. In most of the cases, solutions with an average misfit angle higher than 25° (6b, 17, 23) also show large confidence regions for at least one of the principle stress axes. Some boxes show exceptions for these dependencies between the size of confidence regions and quality assessment. Box 16 (Mbeya), for example, has the highest maximum average misfit  $\alpha$  in this study, but the confidence regions are focused, even though they cover a rather large area in the stereoplot. Because of the oblique orientations of the principle stress axes found with the SLICK method, no regime can be assessed. The results of the TENSOR method, however, indicate a SS regime. Another example for the independence of confidence regions and overall quality is box 10. It has a clearly defined confidence region for the  $\sigma_3$  axis and possible  $\sigma_1$  orientations orthogonal to that. Nevertheless, it has only a C-quality ranking because of the low number of inverted focal mechanisms. Here the focal mechanisms agree for a common stress tensor, but are down ranked since the low number of data allows only for a minor reliability (box 5 shows a similar behaviour).

The boxes with less than 7 data (19–21) show highly scattered confidence regions (Fig. 5) and ambiguous stereograms (Fig. 4). The results obtained may be the best solution for the data given but only with a minor degree of reliability. As a consequence, we assign boxes 19, 20, 21 to D-quality for which the  $S_{\text{Hmax}}$  and  $S_{\text{hmin}}$  are assumed within  $\pm 25$ – $40^\circ$  according to Heidbach et al. (2010-this issue).

Finally, we conclude that when both inversion methods show similar stress orientations and the confidence regions confirm a stable result, the results for these boxes are reliable.

### 6.3. SH orientations

The horizontal stress orientations are usually expressed in terms of  $S_{\text{Hmax}}$  in the World Stress Map and are presented in a similar way in this paper (Figs. 3, 6, 7). Hereafter, for the sake of clarity, we discuss them in terms of  $S_{\text{hmin}}$  for normal faulting (NF) regimes and of  $S_{\text{Hmax}}$  for thrust faulting (TF) regimes.

Our stress inversion results reveal a general trend of E–W extension for all over East Africa (Fig. 6). However, two dominant NF stress regimes are distinguishable for the EARS: an WN–ESE  $S_{\text{hmin}}$  orientation characterises the north-western segments of the EARS (Main Ethiopian Rift: box 5, Albertine Rift: box 11, Kivu Rift: box 12), and South-western High Plateau region (Luangwa Graben: box 20, Mweru Graben: box 21, Upemba Graben: box 22), while an ENE–WSW  $S_{\text{hmin}}$  orientation is typical for the southernmost rift segment (Malawi Rift: box 17, Central Mozambique: box 18), the continental margin (Indian Coast: box 7, Mozambique Channel: box 8, Madagascar: box 9), the central part of the Western Rift Branch (South-Tanganyika: box 14, Rukwa: box 15), and the southern extremity of the Eastern Rift Branch (Manyara–Dodoma Rift: box 6b). Within the EARS, only the Natron Rift (box 6a) and Mbeya Triple Junction show nearly N–S trending  $S_{\text{hmin}}$ , but outside the rift, also South Sudan (box 10), Congo River Basin (box 23) and South Africa (box 19) show nearly N–S  $S_{\text{hmin}}$ . For the extreme north-west of the studied region, the  $S_{\text{hmin}}$  orientation is orthogonal to the trend of the Red Sea (box 1) and to the N–S scarp bordering the western side of the Afar depression (box 2), and slightly oblique to the Gulf of Aden basin (Box 4). A rapid lateral anticlockwise change in  $S_{\text{hmin}}$  orientation is observed from the Western Afar (box 2) to the Afar depression (box 3).

Fig. 7 shows stress data of the World Stress Map (WSM) database (Müller et al., 2003; Heidbach et al., 2010-this issue), together with the results of this study presented as average  $S_{\text{Hmax}}$  orientations

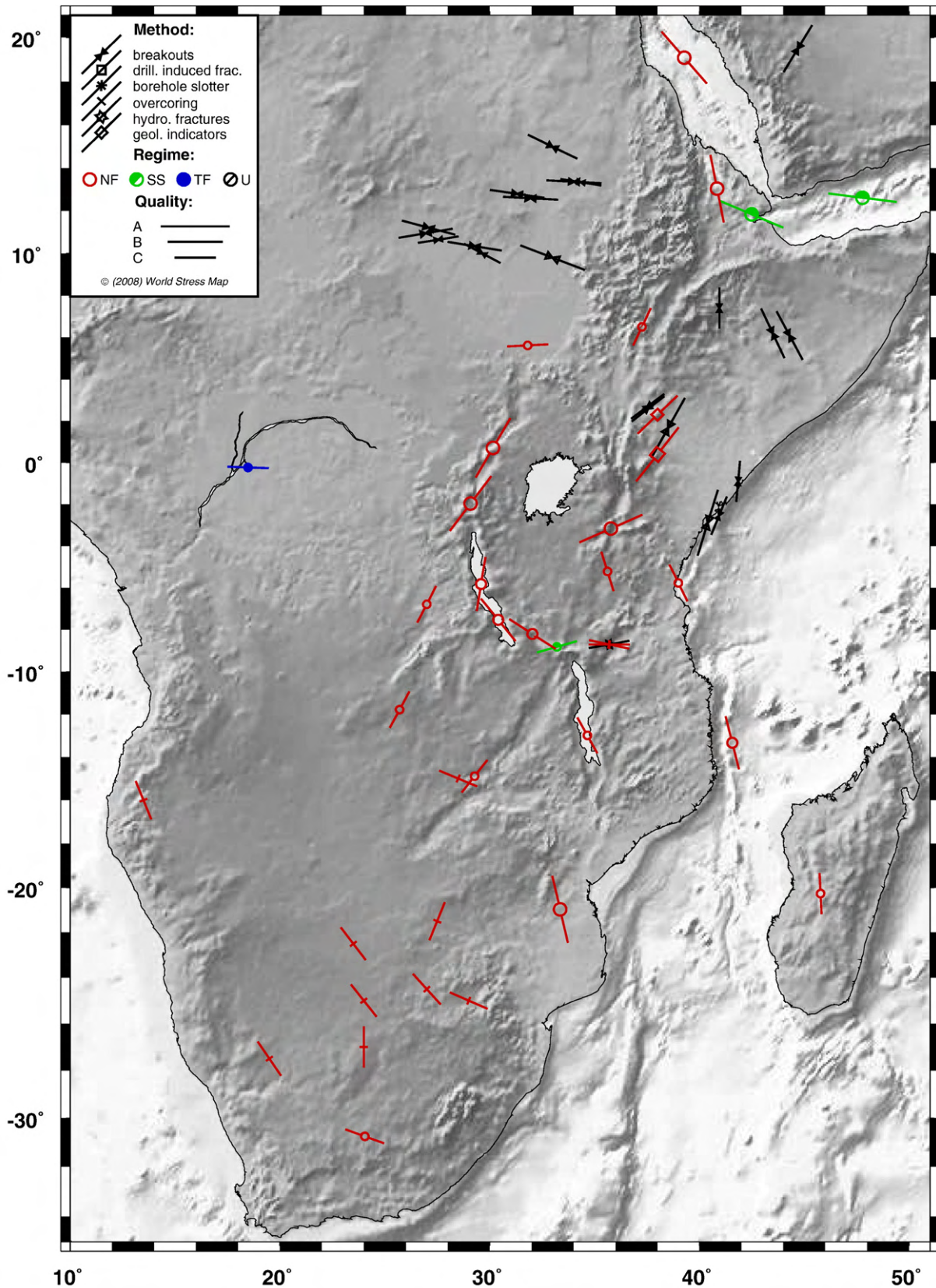


Fig. 7. Synthesis of the horizontal stress orientations ( $S_{Hmax}$ ) combining the results from this study (circles, average from both methods) and World Stress Map release 2008 (other symbols – single focal mechanism solutions excluded, Heidbach et al., 2010-this issue). Colours represent stress regimes. Details about regime, quality and type of data: see legend.

of both formal inversion methods. Beside single focal mechanism solutions, the WSM contains stress data from geological field observations, orientations determined from borehole overcoring and

breakout analyses. The stress orientations of the WSM support the general trend of E–W extension (N–S  $S_{Hmax}$ ) for the EARS and provide additional data in regions where no or only sparse focal mechanism

data are available. North of the Kenya Rift and on the northern Indian Coast, geological and breakout data indicate ENE–WSW orientations of  $S_{Hmax}$  as also apparent for the Eastern Rift Branch in our results. Together with our result from Lake Natron area (box 6a), it forms a relatively homogeneous province with ENE–WSW to NE–SW  $S_{Hmax}$ , in sharp contrast with the coastal region from Tanzania to Madagascar (boxes 6b to 9) with very consistent WNW–ESE  $S_{Hmax}$ . Breakout data east of the Afar triple junction and the Main Ethiopian Rift show NW–SE oriented  $S_{Hmax}$ , which are roughly parallel to the mountain ranges along the flanks of the Afar triangle and may be due to the dominating topography. West of the Main Ethiopian Rift in Sudan, breakout data witness nearly E–W oriented  $S_{Hmax}$ . It is a wide low-land region west of the EARS belonging to the Somalian plate and affected like in the Congo River Basin (box 23) and in South-Sudan (box 10) by a stable E–W  $S_{Hmax}$  orientation over large distances. Overcoming data in South Africa varies strongly between NW–SE and NE–SW extension and underline the heterogeneity of the stress field in South Africa that also results from our stress inversion.

#### 6.4. Tectonic stress regime

Although the dominant tectonic regime is NF, focal mechanisms of SS type are present in most of the boxes. This is particularly the case in the north-eastern branch of the rift, from the Red Sea to the Gregory Rift (boxes 1–6b). In the other rift basins, one or two SS focal mechanisms are often associated with the NF mechanisms, without apparent incompatibility in terms of the resulting stress orientation.

Most stress inversion results are in a NF regime, with average  $R'$  values ranging from 0.28 to 0.84 (Table 2b). Values close to 0.5 denote a pure NF regime (e.g. 0.48 average value for box the Manyara–Dodoma Rift: box 6b and 0.56 for Central Mozambique: box 18), lower values denote a tendency towards radial extension (0.31 average values for the Kivu Rift: box 12 and 0.28 for the Rukwa Rift: box 15) and higher values indicate the presence of a strike-slip component (e.g. 0.84 average value for Red Sea: box 1, 0.77 for the South-Sudan: box 10, and 0.73 for North-Tanganyika: box 13). Only a few boxes show SS regime, near the Afar triple junction (1.28 for the Afar Depression: box 3, 1.18 for the Gulf of Aden: box 4) and at Mbeya (1.42, box 16) which lies in the position of a triple junction. The large Congo River Basin (box 23) is the only region which shows TF regime with an average  $R' = 2.52$ . Here both, the stereograms (Fig. 4) and the confidence regions (Fig. 5) significantly show the presence of a thrust faulting stress regime but with a rather large confidence region for the  $\sigma_3$  axis.

Low average  $R'$  values were obtained for the eastern part of Africa: 0.48 for Manyara–Dodoma Rift (box 6b), 0.46 for the Indian coast (box 7) and 0.40 for the Mozambique Channel (box 8), but consistently higher values were obtained with both methods for Madagascar (0.65, box 9). This contrasts with the results of Coblenz and Sandiford (1994) that show compression in the oceanic basins all around Africa in general and in the Mozambique Channel in particular.

For a large part of the Western Rift Branch (boxes 11–15 and 17), pure NF prevail with a slight radial component (average  $R' = 0.42$ ), as indicated by both methods. As an exception, the Mbeya region (Box 16) has a significantly higher  $R'$  value (1.42 with Tensor, undetermined but either NF or SS with SLICK) than in the adjacent Rukwa and Malawi rifts. This indicates mixed strike-slip and normal faulting, consistent with geological fault-slip data from Late Quaternary sediments and volcanics (Delvaux et al., 1992 and more recent unpublished data).

Interestingly, the three boxes for the South-western High Plateau region (boxes 20–22) show relatively high  $R'$  values (0.57–0.62) in comparison with the Western Rift (0.42 in average, boxes 11–15, 17–18) and the Eastern Rift (0.48 in average, boxes 5–9). In spite of the low data content of boxes 20–22 this might suggest a different process for the opening of the grabens in the South-western High Plateau region than the one operating in the rest of the EARS.

Further west, the Congo River Basin (box 23) is affected by a pure TF stress field ( $R' = 2.52$ ) that differs from the model of Coblenz and Sandiford (1994) showing a neutral state of stress in this region. This type of stress field with an E–W  $S_{Hmax}$  seems to affect a large portion of the Nubian plate. In South Sudan the 1990 seismic crisis also gives an E–W  $S_{Hmax}$  but a NF regime with a marked strike-slip component ( $R' = 0.77$ ). Further North in Sudan, the breakout data of the WSM still indicate E–W  $S_{Hmax}$  but without indication on the stress regime (Fig. 7). In South Africa, our inversion results again show E–W  $S_{Hmax}$  but the WSM data are less consistent.

In the extreme north-west, the tectonic regime is NF for both the Red Sea (box 1) and Western Afar (box 2) where extension is almost orthogonal to the trend of the extensional structures, while it is SS for the Afar Depression (box 3) and Red Sea (box 4) where the extension is oblique to the main structures.

#### 6.5. Driving forces

First-order stress pattern in continents are a consequence of plate boundary forces, while second order pattern might be related to intralithospheric processes and to gravitational potential of topography as discussed by several authors for the African continent (Pavoni, 1992; Zoback, 1992b; Coblenz and Sandiford, 1994; Bird et al., 2006). Coblenz and Sandiford (1994) performed a two-dimensional finite element modelling using multi-layered vertical columns with varying densities and a spatial resolution of 2°, driven solely by intraplate gravitational PE. Stamps et al. (submitted for publication) present a new analysis, more accurate and with a higher resolution, using a thin sheet approach and the CRUST 2.0 model, also driven by horizontal gradients of gravitational PE. Both models show that the large-scale extensional stress field in eastern and southern Africa can be the action of gravitational potential energy within the plates. As a consequence, in the absence of rifting, the stress field in the African plate would be dominantly compressional as Africa is surrounded by spreading oceanic ridges and an orogenic boundary to the north.

The ENE–WSW  $S_{Hmax}$  orientations computed match well with the results of the present study in the South-western High Plateau region (boxes 20–22: Upemba, Mweru and Luangwa grabens) and along the north-western part of the rift. However, their two-dimensional model cannot resolve the details of the stress orientations and regime we find in the EARS, in particular the radial extension in the rift basins surrounding Tanzanian craton (Victoria plate) and the consistent extensional regime along the Indian Coast, and Mozambique Channel (TF against NF in this study, boxes 7–8). Also, our results show a more compressional stress regime for the Congo River Basin (neutral in the models against TF in our study, box 23) and the Mozambique Channel.

For the second and third order stress pattern, we find that the horizontal stress axes within the EARS are often orthogonal to the trend of the rift basins. This is an important and new result, as Foster and Jackson (1998) and Calais et al. (2006) stressed that the earthquake slip vector directions vary little along the major segments of the EARS. In our study we use a new focal mechanism dataset that includes considerably more data than earlier studies—especially for earthquakes with magnitudes below  $M_w$  5 (Ferdinand and Arvidsson, 2002b; Barth et al., 2007). Additionally, we performed a formal stress inversion that allows a more detailed analysis than regarding single focal mechanism solutions as it was done in previous studies. The radial pattern of  $S_{hmin}$  orientations around the Tanzanian craton (Fig. 6) is consistent with the model of Weeraratne et al. (2003). They show that the necessary buoyancy for supporting the regional uplift of the East African Plateau can be provided by the spreading of a mantle plume head beneath the Tanzanian craton. The seismic anisotropy data of Weeraratne et al. (2003) can be best explained by a model with a radial pattern of azimuthal anisotropy, suggesting a possible outward flow of the plume away from the cratonic keel. The Tanzanian craton also corresponds to the Victoria plate identified by Calais et al.

(2006) on the basis of GPS and earthquake slip vector data. It is almost surrounded by rift basins that mark the boundary with the surrounding plates (Nubian plate to the west and north, Somalian plate to the east, and Rovuma plate to the south after Calais et al., 2006). In our results, there is a marked tendency of the computed  $S_{Hmax}$  orientations to be parallel to these basins (and  $S_{Hmin}$  orthogonal to them: boxes 13–17 for the Western Branch and boxes 7–8 for the Eastern Branch). This point to a sub-orthogonal opening of these basins rather than oblique or even strike-slip opening as proposed by a number of authors (Kazmin, 1980; Tiercelin et al., 1988; Chorowicz, 1989, 2005; Wheeler and Karson, 1994). In this respect, the data of Ferdinand and Arvidsson (2002b) are particularly interesting as they show clearly that the southern extremity of the Rukwa Rift is opening in an orthogonal way. This is also confirmed by the presence of the large Kanda active fault system (Vittori et al., 1997) as by unpublished geological fault-slip data measured along this fault (Delvaux et al., 2007). The sub-orthogonal opening of the Rukwa basin is also a key factor in the proposed counter-clockwise rotation of the Victoria plate relative to Nubia (Calais et al., 2006).

The lowlands of the Somalian plate, where data are available, show a consistent E–W orientation of  $S_{Hmax}$ , with even a compressional regime in the Congo River Basin. This could reflect the first order stress pattern of the African plate, far from the effects of the East African Rift System and its elevated regions. The African plate is effectively surrounded by spreading ridges on the western, southern and eastern sides, and by an orogenic collision to the North. As shown by Zoback (1992a), most of the continent interiors are affected by compressional stresses. In the case of the African plate, we would expect a similar pattern in the absence of the EARS. The striking difference between the stress pattern of the Somalian lowlands and the EARS highlands points to a major impact of the EARS on the African stress pattern, responsible for the widespread extensional stresses within a continental plate which otherwise would probably be affected by general E–W compression.

## 7. Conclusion

We show that using focal mechanism data of 332 earthquakes in the African plate, it is possible to resolve the first and second order stress field of the East African Rift by formal stress inversion. For some distinct regions we even obtain information on the local third order stress pattern. Both techniques used; the TENSOR method (Delvaux and Sperner, 2003) and the SLICK method (Michael, 1984/1987), show very similar results of the  $S_{Hmax}$  orientation. Only for boxes that contain a low number of focal mechanisms the orientations vary significantly. Differences in the stress ratio larger than 0.2 are found in a few boxes. However, the uncertainties in the stress regime determination are not related to the number of data used.

In terms of stress orientations, the eastern part of the African plate, which is dominated by the EARS, is affected by stresses with a general E–W orientation of horizontal principal extension ( $S_{Hmin}$ ), while the Nubian plate is affected by E–W horizontal principal compression ( $S_{Hmax}$ ). While most of the rift basins that surround the Tanzanian craton display  $S_{Hmin}$  orientations roughly orthogonal to their trend, two dominant trends of  $S_{Hmin}$  arise: WNW–ESE extension in the north-western segments of the EARS and in the South-western High Plateau region and ENE–WSW extension in the central part of the Western Rift Branch, the southern extremity of the Eastern Rift Branch, the southernmost rift segment and the continental margin.

The tectonic stress regime observed show some discrepancies with the modelled one. Normal faulting is as expected found in conjunction to the broad uplifts associated with most part of the rift, confirming the importance of the gravitational PE forces in the center of the continent. However, the low continental lands along the Indian Coast and the Mozambique Channel portion of the Indian oceanic plate are affected by extensional faulting while the Congo River Basin on the western side of the rift is characterized by thrust faulting regime.

Thanks to the relatively high density of data available, we show that the 2nd and 3rd order stresses might show rapid lateral variations, probably reflecting a complex 3-dimensional crustal structure and/or lithospheric plate architecture. The discrepancies that arise between our results and the stress pattern predicted by the models driven by gravitational PE forces only may suggest an overestimation of the continental PE forces in the models. We conclude that additional sources of tectonic stresses are necessary to explain the observed patterns. These might reflect deep processes like the spreading of a mantle plume head beneath the Tanzanian craton (Weeraratne et al., 2003) or mantle flow at the base of the lithosphere (Calais et al., 2006), or a combination of both.

## Acknowledgements

Damien Delvaux is funded by the SPP Belgian Science Policy under Action 1 program, this work being performed under project TectoSedi-Congo. We thank the Royal Museum for Central Africa for active support all along this work. The manuscript benefited from the constructive comments of an anonymous reviewer as from the encouragements of the Editor, Mike Sandiford.

## References

- Abeinomuigisha, D., 2007. Current understanding of the tectonic setting of the Albertine Graben, East African Rift System. Internal Conference on the East African Rift System (EARS-07), Kampala, 23–25 July 2007, Abstract volume, 28–29.
- Abeinomuigisha, D., Mugisha, F., 2004. Structural analysis of the Albertine Graben, Western Uganda. East African Rift System Evolution, Resources and Environmental Conference, Addis Ababa, 20–24 June 2004, Extended Abstracts, 4–6.
- Angelier, J., 1991. Inversion directe de recherche 4-D: comparaison physique et mathématique de deux méthodes de détermination des tenseurs des paléocontraintes en tectonique de failles. C.R. Acad. Sci., Paris 312 (II), 1213–1218.
- Arvidsson, R., Ekström, G., 1998. Global CMT analysis of moderate earthquakes,  $M_w \geq 4.5$ , using intermediate-period surface waves. Bull. Seism. Soc. Am. 88 (4), 1003–1013.
- Ayele, A., 2002. Active compressional tectonics in Central Africa and implications for plate tectonic models: evidence from fault mechanism studies on the 1998 earthquakes in the Congo Basin. J. Afr. Earth Sci. 35, 45–50.
- Barth, A., 2007. Frequency sensitive moment tensor inversion for light to moderate magnitude earthquakes in eastern Africa and derivation of the regional stress field. PhD thesis, University of Karlsruhe.
- Barth, A., Wenzel, F., Giardini, D., 2007. Frequency sensitive moment tensor inversion for light to moderate magnitude earthquakes in eastern Africa. Geophys. Res. Lett. 34, L15302.
- Barth, A., Wenzel, F., 2010. New constraints on the intraplate stress field of the Amurian plate deduced from low magnitude earthquake focal mechanisms. Tectonophysics 482 (1–4), 160–169.
- Bird, P., Ben-Avraham, Z., Schubert, G., Andreoli, M., Viola, G., 2006. Patterns of stress and strain rate in southern Africa. J. Geophys. Res. 111, B08402.
- Bosworth, W., Strecker, M.R., 1997. Stress changes in the Afro-Arabian rift system during the Miocene to Recent period. In: Fuchs, K., Altherr, R., Müller, B., Prodehl, C. (Eds.), Stress and stress release in the lithosphere of the Afro-Arabian rift system: Tectonophysics, vol. 278(1–4), pp. 47–62.
- Bosworth, W., Strecker, M.R., Blisniuk, P.M., 1992. Integration of East African paleostress and present-day stress data: implications for continental stress field dynamics. J. Geophys. Res. 97 (B8), 11,851–11,865.
- Bott, M.H.P., 1959. The mechanisms of oblique slip faulting. Geol. Mag. 96, 109–117.
- Brazier, R.A., Nyblade, A.A., Florentin, J., 2005. Focal mechanisms and stress regime in NE and SW Tanzania, East Africa. Geophys. Res. Lett. 32, L14315.
- Calais, E., Ebinger, C., Hartnady, C., Nocquet, J.M., 2006. Kinematics of the East African Rift from GPS and earthquake vector data. In: Yirgu, G., Ebinger, C.J., Maguire, P.K.H. (Eds.), The Afar volcanic province within the East African Rift System: Geol. Soc. Lond. Spec. Publ., vol. 259, pp. 9–22.
- Calais, E., d'Oreye, N., Albaric, J., Deschamps, A., Delvaux, D., Déverchère, J., Ebinger, C., Wambura, R.F., Kervyn, F., Macheyeky, A.S., Oyen, A., Saria, E., Smets, B., Stamps, D.S., Wauthier, C., 2008. Aseismic strain accommodation by dyking in a youthful continental rift. East Afr. Nature 456 (11), 783–787. doi:10.1038/nature07478.
- Camelbeeck, T., Iranga, M.D., 1996. Deep crustal earthquakes and active faults along the Rukwa trough, Eastern Africa. Geophys. J. Int. 124, 612–630.
- Casey, M., Ebinger, C., Keir, D., Gloagen, R., Mohamed, F., 2006. Strain accommodation in transitional rifts: extension by magma intrusion and faulting in the Ethiopian rift magmatic segment. In: Yirgu, G., Ebinger, C.J., Maguire, P.K.H. (Eds.), The Afar volcanic province within the East African Rift System: Geol. Soc. Lond. Spec. Publ., vol. 259, pp. 143–163.
- Chorowicz, J., 1989. Transfer and transform fault zones in continental rifts: examples in the Afro-Arabian rift system. Implications of crust breaking. J. Afr. Earth Sci. 8, 203–214.
- Chorowicz, J., 2005. The East African Rift System. J. Afr. Earth Sci. 43, 79–410.

- Chorowicz, J., Mukonki, M.B., 1980. Linéaments anciens, zones transformantes récentes et géotectonique des fossés dans l'est Africain, d'après la télédétection et la microtectonique. *Mus. roy. Afr. centr., Tervuren (Belg.), Dépt. Géol. Min., Rapp. ann.* 1979, 143–146.
- Chu, D.H., Gordon, R.G., 1999. Evidence for motion between Nubian and Somalia along the Southwest Indian Ridge. *Nature* 298, 64–66.
- Coblentz, D.D., Sandiford, M., 1994. Tectonic stresses in the African plate: Constraints on the ambient lithospheric stress state. *Geology* 22, 831–834.
- Daly, M., Lawrence, S., Diemu-Tshiband, K., Matouana, B., 1992. Tectonic evolution of the Congo River Basin, Zaire. *J. Geol. Soc.(Lond.)* 149, 539–546.
- De Bremaeker, J.-Cl., 1956. Premières données sismologiques sur le Graben de l'Afrique Centrale. *Acad. R. Sci. Coloniales, Bull. II-1956* 4, 762–787.
- Delvaux, D., 1991. The Karoo to Recent rifting in the western branch of the East-African Rift System: A bibliographical synthesis. *Mus. roy. Afr. centr., Tervuren (Belg.), Dépt. Géol. Min., Rapp. ann.* 1989–1990, 63–83.
- Delvaux, D., 1993. Quaternary stress evolution in East Africa from data of the western branch of the East African rift. In: Thorweih, Schandelmeier (Eds.), *Geoscientific Research in Northern Africa, Balkema, Rotterdam*, pp. 315–318.
- Delvaux, D., Hanon, M., 1993. Neotectonics of the Mbeya area, SW Tanzania. *Mus. roy. Afr. centr., Tervuren (Belg.), Dépt. Géol. Min., Rapp. ann.* 991–1992, 87–97.
- Delvaux, D., Sperner, B., 2003. Stress tensor inversion from fault kinematic indicators and focal mechanism data: the TENSOR program. In: Nieuwland, D. (Ed.), *New Insights into Structural Interpretation and Modelling: Geol. Soc. Lond. Spec. Publ.*, vol. 212, pp. 75–100.
- Delvaux, D., Levi, K., Kajara, R., Sarota, J., 1992. Cenozoic paleostress and kinematic evolution of the Rukwa–North Malawi rift valley (East African Rift System). *Bull. Centres Rech. Expl. Prod. Elf Aquitaine* 16/2, 383–406.
- Delvaux, D., Moeys, R., Stapel, G., Petit, C., Levi, K., Miroshnichenko, A., Ruzhich, V., Sankov, V., 1997. Paleostress reconstructions and geodynamics of the Baikal region, Central Asia. Part II: Cenozoic rifting. In: Cloetingh, S., Fernandez, M., Munoz, J.A., Sassi, W., Horvath, F. (Eds.), (Editors), *Structural Controls on Sedimentary Basin Formation: Tectonophysics*, vol. 282, pp. 1–38.
- Delvaux, D., Kervyn, R., Vittori, E., Kajara, R.S.A., Kilembe, E., 1998. Late Quaternary tectonic activity and lake level fluctuation in the Rukwa rift basin, East Africa. *J. Afr. Earth Sci.* 26, 397–421.
- Delvaux, D.A.S., Macheyeki, A.S., Kervyn, F., Petermans, T., Verbeeck, K., Temu, E.B., 2007. Earthquake geology of the Kanda fault system (Tanganyika–Rukwa rift, SW highlands of Tanzania). EGU General Assembly 2007, Vienna, Session TS3.3/NH4.4 – Earthquake Geology. *Geophys. Res. Abstr.* 9, 09129.
- Doser, D.I., Yarwood, D.R., 1991. Strike-slip faulting in continental rifts: examples from Sabukia, East Africa (1928), and other regions. *Tectonophysics* 197, 213–224.
- Downey, N.J., Gurnis, M., 2009. Instantaneous dynamics of the cratonic Congo basin. *Journal of Geophysical Research, Solid Earth*, 2008JB006066R.
- Dziewonski, A.M., Ekström, G., Franzen, J.E., Woodhouse, J.H., 1987. Global seismicity of 1977: centroid-moment tensor solutions for 471 earthquakes. *Phys. Earth Planet. Inter.* 45, 11–36.
- Ebinger, C.J., 1989. Geometric and kinematic development of border faults and accommodation zones, Kivu–Rusizi Rift, Africa. *Tectonics* 8 (1), 117–133.
- Ebinger, C., Casey, M., 2001. Continental breakup in magmatic provinces: an Ethiopian example. *Geology* 29, 525–530.
- Ebinger, C.J., Deino, A.L., Drake, R.E., Thesa, A.L., 1989. Chronology of volcanism and rift basin propagation: Rungwe volcanic provinces, East Africa. *J. Geophys. Res.* 94 (B11), 15,783–15,803.
- Fairhead, J.D., Girdler, R.W., 1971. The seismicity of Africa. *Geophys. J. R. Astron. Soc.* 24, 217–301.
- Fairhead, J.D., Stuart, G.W., 1982. Seismicity of the East-African Rift System and comparison with other continental rifts. In: Palmason, G. (Ed.), *Continental and Oceanic Rifts: Geodynamic series*, vol. 8, pp. 41–61.
- Fenton, C.H., Bommer, J.J., 2006. The Mw 7 Machaze, Mozambique, earthquake of 23 February 2006. *Seismol. Res. Lett.* 77, 426–439.
- Ferdinand, R.W., Arvidsson, R., 2002a. The determination of source mechanisms of small earthquakes and revised models of local crustal structure by moment tensor inversion. *Geophys. J. Int.* 151, 221–234.
- Ferdinand, R.W., Arvidsson, R., 2002b. The influence of local topographic relief on regional stress: an example from the Rukwa Rift, Tanzania. *Investigations of Crustal Structure and Seismo-tectonics in the Western Branch of the East African Rift System: Comprehensive Summaries of Uppsala Dissertations from the Faculty of Sciences and Technology*, vol. 783, pp. 2–12.
- Fernandez, R.M.S., Ambrosius, B.A.C., Noomen, R., Bastos, L., Combrinck, L., Miranda, J.M., Spakman, W., 2004. Angular velocities of Nubia and Somalia from continuous GPS data: implications on present-day relative kinematics. *Earth Planet. Sci. Lett.* 222, 197–208.
- Foster, A.N., Jackson, J.A., 1998. Source parameters of large African earthquakes: implications for crustal rheology and regional kinematics. *Geophys. J. Int.* 134, 422–448.
- Gaulon, R., Chorowicz, J., Vidal, G., Romanowicz, B., Roult, G., 1992. Regional geodynamic implications of the May–July 1990 earthquake sequence in southern Sudan. *Tectonophysics* 209, 87–103.
- Garfunkel, Z., Beyth, M., 2006. Constraints on the structural development of Afar imposed by the kinematics of the major surrounding plates. In: Yirgu, G., Ebinger, C.J., Maguire, P.K.H. (Eds.), *The Afar Volcanic Province Within the East African Rift System: Geol. Soc. Lond. Spec. Publ.*, vol. 259, pp. 23–42.
- Gephart, J.W., Forsyth, D.W., 1984. An improved method for determining the regional stress tensor using earthquake focal mechanism data: application to the San Fernando earthquake sequence. *J. Geophys. Res.* 89 (B11), 9305–9320.
- Giardini, D., 1999. The global seismic hazard assessment program (GSHAP) 1992/1999. *Ann. Geofis.* 42 (6), 957–974.
- Girdler, R.W., McConnell, D.A., 1994. The 1990 to 1991 Sudan Earthquake Sequence and the Extent of the East African Rift System. *Science* 264, 67–70.
- Grimson, N.L., Chen, W.P., 1988. Earthquakes in Davie Ridge–Madagascar region and the southern Nubian–Somalian plate boundary. *J. Geophys. Res.* 93 (B9), 10,439–10,450.
- Heidbach, O., Tingay, M., Barth, A., Reinecker, J., Kurfeß, D., Müller, B., 2010. Global spatial wave-length analysis of the tectonic intraplate stress pattern. *Tectonophysics* (this issue).
- Horner-Johnson, B.C., Gordon, R.G., Cowles, S.M., Argus, D.F., 2005. The angular velocity of Nubia relative to Somalia and the location of the Nubia–Somalia–Antarctica triple junction. *Geophys. J. Int.* 162, 221–238.
- Ibs-von Seht, M., Blumenstein, S., Wagner, R., Hollnack, D., Wohlenberg, J., 2001. Seismicity, seismotectonics and crustal structure of the southern Kenya Rift–new data from the Lake Magadi area. *Geophys. J. Int.* 146, 439–453.
- Jackson, J., Blenkinsop, T., 1993. The Malawi earthquake of March 10, 1989: deep faulting within the East African Rift System. *Tectonics* 12, 1131–1139.
- Jackson, J., Blenkinsop, T., 1997. The Bilila–Mtakataka fault in Malawi: an active, 100-long, normal fault segment in thick seismogenic crust. *Tectonics* 16, 137–150.
- Karner, G.D., Byamungu, B.R., Ebinger, C.J., Kampunzu, A.B., Mukasa, R.K., Nyakaana, J., Rubondo, E.N.T., Upcott, N.M., 2000. Distribution of crustal extension and regional basin architecture of the Albertine rift system, East Africa. *Mar. Pet. Geol.* 17, 1131–1150.
- Kazmin, V., 1980. Transform faults in the East African Rift System. *Geodynamic Evolution of the Afro-Arabian Rift System: Accademia Nazionale dei Lincei, Roma. Atti dei convegni Lincei*, vol. 47, pp. 65–73.
- Kebede, F., Kulhanek, O., 1991. Recent seismicity of the East African Rift System and its implications. *Phys. Earth Planet. Inter.* 68, 259–273.
- Kilembe, E.A., Rosendahl, B.R., 1992. Structure and stratigraphy of the Rukwa Basin. *Tectonophysics* 209, 143–158.
- Koehn, D., Aanyu, K., Haines, S., Sashau, T., 2008. Rift nucleation, rift propagation and the creation of basement micro-plates within active rifts. *Tectonophysics* 458, 105–116.
- Laerdal, T., Talbot, M.R., 2002. Basin neotectonics of Lakes Edward and George, East African Rift. *Palaeogeogr. Palaeoclimatol. Palaeoecol.* 187, 213–232.
- Le Gall, B., Vétel, W., Morley, C., 2005. Inversion tectonics during continental rifting: the Turkana Cenozoic rifted zone, Northern Kenya. *Tectonics* 24, TC2002. doi:10.1029/2004TC001637.
- Lemaux, J., Gordon, R.G., Royer, J.-Y., 2002. The location of the Nubia–Somalia boundary along the Southwest Indian Ridge. *Geology* 30, 339–342.
- Lund, B., Townend, J., 2007. Calculating horizontal stress orientations with full or partial knowledge of the tectonic stress tensor. *Geophys. J. Int.* 270, 1328–1335.
- Macheyeki, A.S., Delvaux, D., De Batist, M., Mruma, A., 2008. Fault kinematics and tectonic stress in the seismically active Manyara–Dodoma Rift segment in Central Tanzania – implications for the East African Rift. *J. Afr. Earth Sci.* 51, 163–188.
- Michael, A.J., 1984. Determination of stress from slip data: faults and folds. *J. Geophys. Res.* 89 (B13), 11517–11526.
- Michael, A.J., 1987. Use of focal mechanisms to determine stress: a control study. *J. Geophys. Res.* 92 (B1), 357–368.
- Midzi, V., Hlatywayo, D.J., Chapola, L.S., Kebede, F., Atakan, K., Lombe, D.K., Turjomurugendo, G., Tugume, F.A., 1999. Seismic hazard assessment in Eastern and Southern Africa. *Annali di Geofisica* 42, 1067–1083.
- Morley, C.K., Cunningham, S.M., Harper, R.M., Wescott, W.A., 1992. Geology and geophysics of the Rukwa rift, East Africa. *Tectonics* 11, 68–81.
- Morley, C.K., Harper, R.M., Wigger, S.T., 1999. Tectonic inversion in East Africa. In: Morley, C.K. (Ed.), *Geoscience of Rift Systems – Evolution of East Africa: AAPG Studies in Geology*, vol. 44, pp. 193–210.
- Morley, C.K., Vanhauwaert, P., De Batist, M., 2000. Evidence for high-frequency cyclic fault activity from high-resolution seismic reflection survey, Rukwa Rift, Tanzania. *J. Geol. Soc.(Lond.)* 157, 983–994.
- Müller, B., Wehrle, V., Hettel, S., Sperner, B., Fuchs, K., 2003. A new method for smoothing oriented data and its application to stress data. In: Ameen, M. (Ed.), *Fracture and In-situ Stress Characterisation of Hydrocarbon Reservoirs: Geol. Soc. Lond. Spec. Publ.*, vol. 209, pp. 107–126.
- Nicholas, C.J., Pearson, P.N., McMillan, I.K., Ditchfield, P.W., Singano, J.M., 2007. Structural evolution of southern coastal Tanzania since the Jurassic. *J. Afr. Earth Sci.* 48 (4), 273–297.
- Nyblade, A.A., Langston, C.A., 1995. East-African earthquakes below 20-km depth and their implications for crustal structure. *Geophys. J. Int.* 121 (1), 49–62.
- Pasyanos, M.E., Nyblade, A.A., 2007. A top to bottom lithospheric study of Africa and Arabia. *Tectonophysics* 444, 27–44.
- Pavoni, N., 1992. Rifting of Africa and pattern of mantle convection beneath the African plate. *Tectonophysics*, 215, 35–53.
- Ring, U., Betzler, C., Delvaux, D., 1992. Normal vs. strike-slip faulting during rift development in East Africa: the Malawi Rift. *Geology* 20, 1015–1018.
- Robert, M., 1956. *Géologie et géographie du Katanga*. Hachez, Bruxelles. 620 p.
- Sander, S., Rosendahl, B.R., 1989. The geometry of rifting in Lake Tanganyika, East-Africa. *J. Afr. Earth Sci.* 8, 323–354.
- Sebagenzi, M.N., Kaputo, K., 2002. Geophysical evidences of continental breakup in the southeast of the Democratic Republic of Congo and Zambia (Central Africa). EGU Stephan Mueller Special Publication Series, vol. 2, pp. 193–206.
- Shudofsky, G.N., 1985. Source mechanisms and focal depths of East African earthquakes using Rayleigh-wave inversion and body-wave modelling. *Geophys. J. R. Astr. Soc.* 83, 563–614.
- Stamps, D.S., Calais, E., Saria, E., Hartnady, C., Nocquet, J.-M., Ebinger, C., Fernandez, R.M., 2008. A kinematic model for the East African Rift. *Geophys. Res. Lett.* 35, L05304.
- Stamps, D.S., Flesch, L.M., Calais, E., Submitted for publication. Lithospheric Buoyancy Stresses in Africa from a This Sheet Approach. *International Journal of Earth Sciences*.

- Strecker, M.R., Blisniuk, P.M., Eisbacher, G.H., 1990. Rotation of extension direction in the central Kenya Rift. *Geology* 18, 299–302.
- Tiercelin, J.J., Chorowicz, J., Bellon, H., Richert, J.P., Mwambene, J.T., Walgenwitz, F., 1988. East Africa Rift System: offset, age, and tectonic significance of the Tanganyika–Rukwa–Malawi intracontinental transcurrent fault zone. *Tectonophysics* 148, 241–252.
- Upcott, N.M., Mukasa, R.K., Ebinger, C.J., 1996. Along-axis segmentation and isostasy in the Western Rift, East Africa. *J. Geophys. Res.* 101 (B2), 3247–3268.
- Vittori, E., Delvaux, D., Kervyn, F., 1997. Kanda Fault: a major seismogenic element west of the Rukwa Rift (East Africa, Tanzania). *J. Geodyn.* 24 (1–4), 139–153.
- Wheeler, W.H., Karson, J.A., 1994. Extension and subsidence adjacent to a “weak” continental transform: an example of the Rukwa Rift, East Africa. *Geology* 22, 625–628.
- Weeraratne, D.S., Forsyth, D.W., Fischer, K.M., Nyblade, A.A., 2003. Evidence for an upper mantle plume beneath the Tanzanian Craton from Rayleigh wave tomography. *J. Geophys. Res.* 108 (B9), 2427. doi:10.1029/2002JB002273.
- Yang, Z., Chen, W.P., 2008. Mozambique earthquake sequence of 2006: High-angle normal faulting in southern Africa. *J. Geophys. Res.* 113 (B12303). doi:10.1029/2007JB005419.
- Zoback, M.L., 1992a. First- and second-order patterns of stress in the lithosphere: the world stress map project. *J. Geophys. Res.* 97 (B8), 11703–11728.
- Zoback, M.L., 1992b. Stress field constraints on intraplate seismicity in eastern North America. *J. Geophys. Res.* 97 (B8), 11761–11782.